Wind Energ. Sci. Discuss., doi:10.5194/wes-2016-22, 2016
Manuscript under review for journal Wind Energ. Sci.
Published: 8 July 2016
© Author(s) 2016. CC-BY 3.0 License.

Improving Lidar-Derived Turbulence Estimates for Wind Energy

Jennifer F. Newman[1] and Andrew Clifton[2]

[1]National Wind Technology Center, National Renewable Energy Laboratory, Golden, CO, 80401, USA
[2]Power Systems Engineering Center, National Renewable Energy Laboratory, Golden, CO, 80401, USA

Correspondence to: Jennifer F. Newman (Jennifer.Newman@nrel.gov)

Abstract.

Remote sensing devices such as lidars are currently being investigated as alternatives to cup anemometers on meteorological towers. Although lidars can measure mean wind speeds at heights spanning an entire turbine rotor disk and can be easily moved from one location to another, they measure different values of turbulence than an instrument on a tower. Current methods for improving lidar turbulence estimates include the use of analytical turbulence models and expensive scanning lidars. While these methods provide accurate results in a research setting, they cannot be easily applied to smaller, commercially available lidars in locations where high-resolution sonic anemometer data are not available. Thus, there is clearly a need for a turbulence error reduction model that is simpler and more easily applicable to lidars that are used in the wind energy industry.

In this work, a new turbulence error reduction algorithm for lidars is described. The algorithm, L-TERRA, can be applied using only data from a stand-alone commercially available lidar and requires minimal training with meteorological tower data. The basis of L-TERRA is a series of corrections that are applied to the lidar data to mitigate errors from instrument noise, volume averaging, and variance contamination. These corrections are applied in conjunction with a trained machine-learning model to improve turbulence estimates from a vertically profiling WINDCUBE v2 lidar.

L-TERRA was tested on data from three sites - two in flat terrain and one in semicomplex terrain. L-TERRA significantly reduced errors in lidar turbulence at all three sites, even when the machine-learning portion of the model was trained on one site and applied to a different site. Errors in turbulence were then related to errors in power through the use of a power prediction model for a simulated 1.5MW turbine. L-TERRA also reduced errors in power significantly at all three sites, although moderate power errors remained for periods when the mean wind speed was close to the rated wind speed of the turbine and periods when variance contamination had a large effect on the lidar turbulence error. Future work will include the use of a lidar simulator to better understand how different factors affect lidar turbulence error and to determine how these errors can be reduced using information from a stand-alone lidar.

1 Introduction

As turbine hub heights increase and wind energy expands to complex and offshore sites, new measurements of the wind resource are needed to inform decisions about site suitability and turbine selection. Currently, most of these measurements are collected by cup anemometers on meteorological (met) towers. Met towers are fixed in location and typically only collect measurements up to and including the height corresponding to the turbine hub height. However, the measurement of wind

Wind Energ. Sci. Discuss., doi:10.5194/wes-2016-22, 2016
Manuscript under review for journal Wind Energ. Sci.
Published: 8 July 2016
© Author(s) 2016. CC-BY 3.0 License.

speeds across the entire turbine rotor disk is extremely important for power estimation (e.g., Wagner et al., 2009), particularly as modern turbines increase in size. In addition, met towers are expensive to construct and maintain; the estimated cost for installing and maintaining an 80m land-based met tower for a 2-year campaign is €92,000 (≈ 105,000 USD; Boquet et al., 2010). In response to the limitations of met towers for wind energy, remote sensing devices such as lidars (light detection and ranging) have been proposed as potential alternatives to cup anemometers on towers. Lidars are now frequently used in the research community (e.g., Barthelmie et al., 2013; Stawiarski et al., 2013; Fuertes et al., 2014; Sathe et al., 2015b), and acceptance of lidars in the wind energy community is increasing. In fact, the use of remote sensing devices for power performance testing in flat terrain is discussed in Annex L of the most recent draft version of IEC 61400-12-1 (International Electrotechnical Commission, 2013).

While lidars are capable of measuring mean wind speeds at several different measurement heights (e.g., Sjöholm et al., 2008; Peña et al., 2009; Barthelmie et al., 2013; Sathe et al., 2015b), they measure different values of turbulence than a cup or sonic anemometer (e.g., Sathe et al., 2011; Newman et al., 2016b). Turbulence, a measure of small-scale fluctuations in the atmospheric flow, is an extremely important parameter in the wind energy industry. Turbulence measurements are used to classify potential wind farm sites and select suitable turbines (International Electrotechnical Commission, 2005) and can also impact power production. Figure 1a shows the response of a modeled 1.5MW turbine to different levels of hub-height turbulence intensity (TI) for the same mean hub-height wind speed. The power produced by the turbine is profoundly impacted by the level of turbulence, particularly near the rated wind speed of the turbine. Because of the paramount importance of turbulence measurements to the wind energy industry, lidars must be able to accurately measure turbulence to be considered a viable alternative to met towers. The inability of lidars to accurately measure turbulence is currently one of the main barriers to replacing met towers with lidars.

In this work, a new turbulence error reduction model, the Lidar Turbulence Error Reduction Algorithm (L-TERRA), was developed for the WINDCUBE v2 (WC) vertically profiling lidar. The model combines physical corrections, such as a spectral correction, with machine-learning techniques to improve lidar turbulence estimates. These estimates are then related to changes in power prediction through the use of a power prediction model. Unlike other methods for improving lidar turbulence estimates, L-TERRA is a simple method that can be easily applied to commercially available lidars. In this paper, the development and initial testing of L-TERRA are discussed.

Results indicate that L-TERRA significantly improves lidar TI and power prediction estimates at three different sites, even when the model is trained at one site and applied to data at a different site. Large errors in power prediction still remain for wind speeds near the rated wind speed of the turbine, where the power curve is extremely sensitive to errors in TI, and for low-shear, high-TI conditions, where variance contamination has a strong impact on lidar TI error. Future work will include the use of a lidar simulator to refine the corrections in L-TERRA and the expansion of L-TERRA to different lidar models and configurations.

Section 2 outlines the main factors that affect lidar turbulence estimates and current methods for improving turbulence estimates. Basic descriptions of L-TERRA and the power prediction model used in this work are given in Section 3. The data sets used to train and test L-TERRA are discussed in Section 4 and the atmospheric conditions present at the different sites are

Wind Energ. Sci. Discuss., doi:10.5194/wes-2016-22, 2016
Manuscript under review for journal Wind Energ. Sci.
Published: 8 July 2016
© Author(s) 2016. CC-BY 3.0 License.

compared. The effects of lidar turbulence error on power prediction at the different sites are described in Section 5. Section 6 includes performance metrics of L-TERRA for all three sites, and atmospheric conditions under which the model requires improvement are highlighted. Conclusions and plans for future work are discussed in Section 7.

2 Background

Although lidars are frequently used in wind energy studies (e.g., Peña et al., 2009; Krishnamurthy et al., 2013; Wharton et al., 2015; Newsom et al., 2015), they typically measure different values of turbulence than a cup or sonic anemometer (e.g., Sathe et al., 2013; Newman et al., 2016b). In this section, the factors that cause these turbulence discrepancies are discussed. In addition, current methods for reducing turbulence measurement error from lidars are highlighted.

2.1 Lidar technology

Lidars emit laser light into the atmosphere and measure the Doppler shift of the backscattered energy to estimate the mean wind velocity of volumes of air. Laser light from Doppler lidars is typically scattered by aerosol particles in the atmosphere, which are normally prevalent in the boundary layer (Emeis, 2010). For pulsed Doppler lidars, the time series of the returned signal is split into blocks that correspond to range gates and processed to estimate the average radial wind speed at each range gate. The sign and magnitude of the radial wind speed are determined from the Doppler shift of the returned signal with respect to the original signal (Huffaker and Hardesty, 1996).

One lidar that is frequently used in the wind energy industry is the WC, manufactured by Leosphere (Orsay, France). The WC employs a Doppler-Beam swinging (DBS) (e.g., Strauch et al., 1984) technique to estimate the three-dimensional wind vector wherein an optical switch is used to point the laser beam toward the four cardinal directions (north, east, south, and west) at an angle of 28° from zenith. The WC also includes a vertical beam position for a direct measurement of the vertical velocity. The WC accumulates measurements at each beam position for one second, such that a full scan takes approximately 4–5 seconds. However, velocity data from the WC are updated each time new information is obtained (i.e., every time the beam moves to a different position), leading to an output frequency of 1 Hz.

2.2 Errors in lidar data

In Doppler wind lidars, instrument noise results from factors such as the limited amount of aerosol scatterers in the probe volume (Lenschow et al., 2000) and spontaneous radiation emissions from the laser (Chang, 2005). Instrument noise increases the variability of the radial wind speeds measured by the lidar, which artificially increases the turbulence estimates. In contrast, volume averaging decreases the turbulence estimated from the lidar. To obtain a reasonable estimate of the radial velocity, lidars require backscatter data from a large number of scatterers within a probe volume. For the WC, the probe volume measures 20 m along the beam and is negligibly small in the cross-beam and vertical directions. The probe volume acts as a low-pass filter, effectively filtering out all turbulent motions that occur on spatial scales smaller than 20 m. The probe volume is a trade-off

Wind Energ. Sci. Discuss., doi:10.5194/wes-2016-22, 2016
Manuscript under review for journal Wind Energ. Sci.
Published: 8 July 2016
© Author(s) 2016. CC-BY 3.0 License.

between spatial resolution and data accuracy; if the probe volume were smaller than 20 m, fewer data points would be available to estimate the radial velocity, and there would be more uncertainty in the measurements.

The WC, like most other commercial lidars, collects measurements around a scanning circle to estimate the three-dimensional wind vector. At each beam position, the WC obtains an estimate of the line-of-sight velocity, which, for the off-vertical beam positions, contains contributions from all three wind components. If it is assumed that the instantaneous flow field is uniform across the scanning circle, then the line-of-sight velocities can be combined to estimate the u, v, and w wind components. However, this assumption is generally not true in turbulent flow, when the wind field changes significantly in both space and time (e.g., Wainwright et al., 2014; Lundquist et al., 2015). As the WC scanning circle has a diameter of 106 m at a measurement height of 100 m above ground level (AGL), it is likely that the instantaneous flow field changes in space, even in flat terrain. This changing flow field across the lidar scanning circle introduces additional terms into the variance calculations in a phenomenon known as variance contamination (e.g., Sathe et al., 2011; Newman et al., 2016b). This effect contaminates the true value of the velocity variance and can cause the lidar to measure higher values of turbulence than a cup or sonic anemometer.

2.3 Current methods for correcting lidar turbulence

Several data processing techniques and state-of-the art measurement configurations have already been developed for acquiring turbulence measurements from lidars (Sathe et al., 2015a). However, many of these measurement configurations require expensive scanning lidars or the fitting of turbulence models that are technically only valid under neutral atmospheric conditions. These techniques are applicable in a research setting, but largely require more instrumentation and measurement data than are typically available during a wind resource assessment.

2.3.1 Fitting a turbulence model

One method for correcting lidar turbulence includes modeling the spatial averaging effects of the lidar probe volume. This method involves convolving the true radial velocity field with a spatial weighting function that is controlled by the lidar beam pattern (e.g., Sjöholm et al., 2009; Sathe et al., 2011). Spatial weighting functions for both pulsed and continuous wave lidars are relatively straightforward (e.g., Sonnenschein and Horrigan, 1971). However, modeling the true velocity field requires knowledge of the three-dimensional turbulence structure, which can be described by the spectral velocity tensor, Φ_{ij}.

The spectral velocity tensor can be modeled through use of the Mann (1994) turbulence model, as in Sjöholm et al. (2009), Mann et al. (2010), Sathe et al. (2011), and others. Fitting the model requires three parameters: a turbulence dissipation rate parameter, a length scale, and a parameter that describes the anisotropy of the flow. Values for these parameters can be estimated by using high-frequency sonic anemometer data, but cannot be obtained from the lidar itself.

2.3.2 Six-beam method

To reduce variance contamination caused by the DBS and Velocity-Azimuth Display (VAD) scans (Browning and Wexler, 1968), Sathe et al. (2015b) proposed a new six-beam scanning technique for Doppler lidars. While the DBS and VAD tech-

Wind Energ. Sci. Discuss., doi:10.5194/wes-2016-22, 2016
Manuscript under review for journal Wind Energ. Sci.
Published: 8 July 2016
© Author(s) 2016. CC-BY 3.0 License.

niques involve using the radial velocities to estimate the u, v, and w wind components, then calculating the variance, the six-beam technique uses the variances of the radial velocities measured at six different beam positions to estimate the variance and covariance components. Newman et al. (2016b) tested the six-beam method with a scanning lidar at the Boulder Atmospheric Observatory (BAO) in Erie, Colorado, and compared six-beam variance estimates to estimates from sonic anemometers on a tower at the site. Newman et al. (2016b) found that while the six-beam method did generally reduce variance contamination in comparison to estimates from a WC lidar that used the DBS technique, errors in the different radial variance estimates caused large errors and even negative values in the resulting u and v variance estimates. Better estimates of the radial velocity variance are likely needed from lidars to obtain accurate results from the six-beam technique.

2.3.3 Multiple lidars

While single lidars require measurements around a scanning circle to estimate the three-dimensional velocity field, multiple scanning lidars can be pointed toward a particular volume of air to obtain turbulence estimates with much higher spatial resolution (e.g., Calhoun et al., 2006; Fuertes et al., 2014; Newsom et al., 2015; Newman et al., 2016a). To collect turbulence measurements, multi-lidar systems must be temporally and spatially synchronized with a high degree of accuracy. Synchronization techniques have been developed for a set of user-customized scanning lidars (Vasiljevic et al., 2014), but are currently not easily implemented on most other scanning lidars. In addition, scanning lidars are much more expensive than commercially available vertically profiling lidars, particularly if more than one scanning lidar is required for operation.

2.3.4 Structure functions

Structure functions describe the spatial correlation of a variable at different separation distances (e.g., Stull, 2000). If the turbulence is isotropic and the turbulence length scale is large, the structure function can be approximated by the Kolmogorov (1941) model and used to estimate the velocity variance. Krishnamurthy et al. (2011) used scanning lidar data from a field campaign to calculate structure functions in both the along-beam and azimuthal directions and fit the functions to the Kolmogorov (1941) model to obtain estimates of the velocity variance. The lidar data used by Krishnamurthy et al. (2011) were obtained from a series of plan-position indicator (PPI) scans with high azimuthal resolution, which is typically not available from a scanning strategy used by a commercially available lidar.

2.3.5 Doppler spectrum

As discussed by Mann et al. (2010), the spectral density of a particular radial velocity, v_r, is essentially a weighted count of all the positions within the probe volume where the radial velocity is equal to v_r. The weighting occurs because the intensity of the lidar beam is highest at the center of the probe volume and drops off for distances in either direction from the probe volume center. The ensemble-averaged spectrum can then be related to the probability density function of the radial velocity at each position within the probe volume. Given this relation, the unfiltered ("true") variance can be obtained from the second central moment of the Doppler spectrum. If the lidar is mounted on a turbine nacelle and pointing upstream, as in Branlard

Wind Energ. Sci. Discuss., doi:10.5194/wes-2016-22, 2016
Manuscript under review for journal Wind Energ. Sci.
Published: 8 July 2016
© Author(s) 2016. CC-BY 3.0 License.

et al. (2013), it can be assumed that the wind field is homogeneous along the lidar beam and that the probability density of v_r is approximately uniform along the probe volume. However, if a ground-based, vertically profiling lidar is used, the mean wind field will not be uniform along the lidar's line-of-sight and the effects of shear must be taken into account when estimating the unfiltered variance from the Doppler spectrum (Mann et al., 2010). Currently, this method is more clearly defined for continuous wave lidars, as the Doppler spectra of pulsed lidars are affected by the finite length of the probe volume in addition to turbulent fluctuations.

2.3.6 Summary

Several methods are currently available for obtaining more accurate turbulence estimates from Doppler lidars. Only a few methods were discussed here; a more extensive discussion of turbulence retrieval techniques can be found in Sathe and Mann (2013) and Sathe et al. (2015a). Most of these methods require the fitting of models and the use of very specific scanning strategies that can currently only be achieved with expensive scanning lidars. The Doppler spectrum method is promising for continuous wave lidars, but requires knowledge of the Doppler spectrum obtained at each lidar beam position, which is usually not available in the output of commercially available systems. Thus, there is clearly a need for a turbulence estimation method that can be implemented on commercially available lidars that use DBS and VAD techniques and that does not require high-resolution data from a sonic anemometer. Details of the new turbulence estimation method proposed in this paper are discussed in the next section.

3 Methodology

The TI error model described in this work, L-TERRA, was initially developed for the WC pulsed Doppler lidar. Future work will involve expanding L-TERRA to different lidar configurations and scanning strategies, although the basic framework for the model will stay the same. The different modules of L-TERRA in its current form are described in this section. In addition, the power prediction model that was used to relate errors in TI to errors in power prediction is introduced.

3.1 TI error model: L-TERRA

A flowchart depicting different methods for correcting TI with L-TERRA is shown in Fig. 2. L-TERRA contains several modules that reduce the lidar TI error in different ways. For each of the main modules, outlined in red in Fig. 2, many different methods are available to reduce the TI error. For example, four different methods were evaluated to reduce noise: a spike filter, and three different methods discussed by Lenschow et al. (2000) (Lenschow 1, Lenschow 2, and Lenschow 3). Some methods can only be applied to the u, v, and w velocity data while others can only be applied to radial velocity data, v_r; thus, two different model paths can be followed for volume averaging and variance contamination, depending on which wind speed parameters are selected to calculate the variance. All possible combinations of different methods were tested on each data set to determine which combination produced the largest reduction in TI and power prediction error.

Wind Energ. Sci. Discuss., doi:10.5194/wes-2016-22, 2016
Manuscript under review for journal Wind Energ. Sci.
Published: 8 July 2016
© Author(s) 2016. CC-BY 3.0 License.

3.1.1 Preprocessing

Several steps are taken before the lidar data enter the TI correction process. First, values of u, v, and w are calculated from the raw WC radial velocity time series. For the WC lidar, the wind speed components can be calculated in two different ways: by estimating new u, v, and w components every time the lidar beam moves to a new position (i.e., every 1 s) or by estimating a single value of each of the wind components for every 4-s scan, similar to a VAD technique. In Section 6, both the 1-s and 4-s techniques are used to calculate the wind components in the evaluation of L-TERRA.

Next, the data are interpolated to a grid with constant temporal spacing, as statistical measures such as the calculation of variance and spectra require that the frequency resolution of the measurements is constant. The mean horizontal wind speed and shear parameter are calculated before L-TERRA is applied, as these parameters are required for implementation of L-TERRA and are relatively unaffected by the errors that plague turbulence measurements.

The 10min mean horizontal wind speed, $\overline{U}$, is defined by Eq. 1:

$$\overline{U} = \overline{(u^2 + v^2)^{1/2}}, \tag{1}$$

where u and v are the east-west and north-south wind components, respectively, and the overbar denotes temporal averaging. The shear parameter, α, is derived from the standard power law equation (International Electrotechnical Commission, 2005):

$$U(z) = U(z_r)\left(\frac{z}{z_r}\right)^{\alpha}, \tag{2}$$

where z is height above ground and z_r is a reference height. Eq. 2 can be simplified by letting $U(z_r)z_r^{-\alpha}$ equal a constant β, as in Clifton et al. (2013). The power law then becomes the following:

$$U(z) = \beta z^{\alpha} \tag{3}$$

A 10min mean value of α can be found by taking the natural logarithm of Eq. 3 and fitting the resulting equation to a straight line. In this work, values of $\overline{U}$ measured by the WC between 40 and 200 m were used to calculate values of α.

The raw wind speeds are rotated into a new coordinate system by forcing $\overline{v}$ and $\overline{w}$ to 0 and aligning u with the 10min mean wind direction (e.g., Kaimal and Finnigan, 1994). The TI is then defined by Eq. 4:

$$TI = \left(\frac{\sigma_u}{\overline{u}}\right) \times 100\%, \tag{4}$$

where σ_u is the standard deviation of u over a 10min period, defined in the new coordinate system, and $\overline{u}$ is the 10min mean wind speed. Eq. 4 gives the initial lidar-estimated value of the horizontal TI. A similar procedure was used to calculate TI from the cup and sonic anemometer data used in this work.

Wind Energ. Sci. Discuss., doi:10.5194/wes-2016-22, 2016
Manuscript under review for journal Wind Energ. Sci.
Published: 8 July 2016
© Author(s) 2016. CC-BY 3.0 License.

3.1.2 Instrument noise

A standard way to remove outliers from a time series is to use a spike filter (e.g., Vickers and Mahrt, 1997). A basic spike filter was evaluated for the model in addition to several methods developed by Lenschow et al. (2000). These methods involve the use of the lidar's velocity spectrum or autocovariance function to estimate the amount of noise in the variance measurements from the lidar.

3.1.3 Volume averaging

Two methods were evaluated to mitigate the effects of volume averaging: structure functions and spectral extrapolation. As discussed in Section 2.3.4, structure functions can be estimated using available lidar data and fit to modeled forms of structure functions to estimate turbulence parameters (e.g., Krishnamurthy et al., 2011). By fitting the lidar data to a model, the reduction of turbulence due to volume averaging is mitigated. Although the estimation of structure functions with a lidar is optimized with the use of a high-resolution PPI scan, as in Krishnamurthy et al. (2011), structure functions can also be estimated from DBS scans.

Another method of mitigating volume averaging is to model the lidar velocity spectrum and use the model to extrapolate the spectrum to higher frequencies. The high-frequency part of the modeled spectrum can then be integrated to obtain an estimate of the variance that is not measured by the lidar as a result of spatial and temporal resolution (e.g., Hogan et al., 2009).

3.1.4 Variance contamination

Methods to reduce variance contamination include the six-beam technique developed by Sathe et al. (2015b), discussed in Section 2.3.2, and the use of Taylor's frozen turbulence hypothesis to estimate the change in the vertical velocity across the lidar scanning circle (Newman, 2015). Variance contamination proved to be the most difficult effect to capture in L-TERRA. Thus, work with a lidar simulator is currently ongoing to make further refinements to this module of L-TERRA.

3.1.5 Machine learning

The previous three modules (instrument noise, volume averaging, and variance contamination) constitute the physics-based corrections of L-TERRA. These modules rely only on data from the lidar itself and use theory rather than mathematical models. While the physics-based corrections do reduce lidar TI error, there is still some error in the lidar TI estimates in comparison to estimates from a cup or sonic anemometer. Thus, machine-learning methods were used in the final step of L-TERRA to bring lidar TI estimates even closer to met tower estimates.

Three machine-learning methods were evaluated as part of L-TERRA: random forests, support vector regression, and multivariate adaptive regression splines (MARS). Random forests were evaluated because they are relatively easy to understand and have previously been used for wind energy applications (e.g., Clifton et al., 2013; Bulaevskaya et al., 2015). Support vector regression and MARS are both well-suited for the prediction of physical processes. More information on random forests, sup-

Wind Energ. Sci. Discuss., doi:10.5194/wes-2016-22, 2016
Manuscript under review for journal Wind Energ. Sci.
Published: 8 July 2016
© Author(s) 2016. CC-BY 3.0 License.

port vector regression, and MARS can be found in Friedman et al. (2001), Smola and Schölkopf (2004), and Friedman (1991), respectively.

Potential predictor variables for the machine-learning models were divided into two broad categories: atmospheric state and lidar operating characteristics. Variables that were evaluated as predictor variables in L-TERRA are given in Table 1. Atmospheric state variables included shear parameter, mean wind speed, Doppler spectral broadening, and u and w velocity variances. Lidar operating characteristics included signal-to-noise ratio (SNR) and internal instrument temperature. Mean wind speed also affects data quality, as lidars cannot measure turbulence at low wind speeds as accurately as a result of relative intensity noise (Chang, 2005). In all, 14 predictor variables were considered for the machine learning portion of L-TERRA.

Sensitivity of the TI error to the various predictor variables was assessed following the guidelines in Annex L of the new committee draft of IEC 61400-12-1 (International Electrotechnical Commission, 2013). Data from the Atmospheric Radiation Measurement (ARM) site, described in Section 4, were used to assess the importance of different predictor variables in predicting lidar TI error. First, predictor variables were binned and bin-means of the TI percent error corresponding to each bin were calculated. A least-squares technique was then used to calculate a regression line between the predictor bin centers and the bin-means of the TI percent error. Sensitivity, defined as the product of the regression line slope and the standard deviation of the predictor variable, was then calculated for each predictor. The sensitivity gives the approximate change in the TI error for a change in the predictor variable that is equivalent to one standard deviation of the variable. All predictor variables had sensitivity values over 0.5, which indicates a significant relationship between all the predictor variables and the TI error, according to Annex L of IEC 61400-12-1 (International Electrotechnical Commission, 2013).

As the majority of the predictor variables are related to the atmosphere, which is a highly synergistic system, it is likely that one or more of the variables are correlated to one another. Thus, a correlation matrix was calculated for the potential predictor variables. For pairs of variables with a correlation coefficient of over 0.5, the predictor with a lower sensitivity value was removed from the list of potential predictor variables. The final predictor variables were as follows: TI from the physics-based corrections, α, SNR, σ_w^2 (w velocity variance), spectral broadening, instrument internal temperature, and pitch of the lidar.

3.2 Power prediction

Reduction in TI error was related to reduction in turbine power prediction error through the use of a power prediction model. Simulations used in Clifton et al. (2013) were again used to develop a power prediction model for the 1.5MW WindPACT turbine (Malcolm and Hansen, 2006). First, 3-D flow fields with varying degrees of wind shear and TI were created using TurbSim (Jonkman, 2009). These flow fields were then used as input for the turbine simulator FAST (Jonkman and Buhl Jr., 2005) to model the response of the WindPACT turbine to flow fields with different degrees of shear and turbulence. The 10min mean hub-height wind speed, hub-height TI, and shear parameter were extracted from the TurbSim output and the 10min mean turbine power was extracted from the FAST output. These parameters, in addition to the turbine operating range, were then used to train a random forest model. The trained model accepts values of mean wind speed, TI, and shear, and predicts the 10min mean power that would be produced by the 1.5MW WindPACT turbine.

Wind Energ. Sci. Discuss., doi:10.5194/wes-2016-22, 2016
Manuscript under review for journal Wind Energ. Sci.
Published: 8 July 2016
© Author(s) 2016. CC-BY 3.0 License.

Lidars can accurately measure the mean wind speed (e.g., Sjöholm et al., 2008; Pichugina et al., 2008; Peña et al., 2009) and the shear parameter, but do not measure the same values of TI as a cup or sonic anemometer (see Section 2.2). Thus, TI is the only variable in the power prediction model that is likely to differ between a lidar and a traditional met tower instrument. In Section 5, values of $\overline{U}$ and α from a WC lidar from three different field campaigns are used as inputs to the power prediction model, in addition to values of TI from both the lidar and collocated sonic and cup anemometers. The difference between the lidar- and sonic- or cup-measured TI is then related to errors in the predicted power.

4 Data sets

L-TERRA was tested on data from three different locations: the Southern Great Plains ARM site in Lamont, Oklahoma; the BAO in Erie, Colorado; and an operational wind farm in the Southern Plains region of the United States (Figs. 3–4). The ARM site, a field measurement site operated by the U.S. Department of Energy, contains several remote sensing and in-situ instruments (Mather and Voyles, 2013). From November 2012 to June 2013, a WC lidar owned by Lawrence Livermore National Laboratory was deployed at the ARM site approximately 100 m from a 60m tower. Gill Windmaster Pro 3-D sonic anemometers are mounted on the tower at 25 and 60 m AGL and collect velocity data at a frequency of 10 Hz.

The BAO is a field site located approximately 25 km east of the Rocky Mountain foothills (Kaimal and Gaynor, 1983). The WC was deployed at the BAO near a 300m tower from February to April 2014. The 300m tower was instrumented with twelve 3-D sonic anemometers, with two sonics mounted on opposite booms every 50 m from 50 to 300 m AGL. RM Young sonics, owned by the University of Oklahoma, were mounted on the northwest booms of the tower, and Campbell Scientific CSAT3 sonics, owned by the National Center for Atmospheric Research, were mounted on the southeast booms.

The WC was also deployed at an operational wind farm in the Southern Great Plains. (Due to a nondisclosure agreement with the wind farm, we cannot disclose the location or details of the wind farm.) The WC was located on the wind farm from November 2013 to July 2014, with a break from February to April 2014 while the WC was located at the BAO. During the wind farm deployments, the WC was sited in the same enclosure as a met tower with standard wind energy instrumentation, including a cup anemometer at the turbine hub height. For the winter deployment, the WC was located near a met tower on the north end of the wind farm, and for the spring/summer deployment, the WC was moved to the tower enclosure at the south end of the wind farm, in accordance with the dominant wind direction during each season at the wind farm. Data shown here are restricted to wind directions corresponding to turbine inflow.

Although the simulated 1.5MW WindPACT turbine used in this work has a hub height of 84 m, none of the sites were instrumented with cup or sonic anemometers at the 84m measurement height. Thus, the closest height to 80 m that contained both lidar and met tower data at each site was defined as the "hub height" for that site. This resulted in hub heights of 60, 100, and 80 m at the ARM site, BAO, and wind farm, respectively.

Histograms of the 10min mean hub-height wind speed, shear parameter, and hub-height SNR from the different sites are shown in Fig. 5. While the ARM site and Southern Plains wind farm experienced similar atmospheric conditions, conditions at the BAO site were characterized by lower values of the mean wind speed, shear parameter, and SNR. Part of this discrepancy,

Wind Energ. Sci. Discuss., doi:10.5194/wes-2016-22, 2016
Manuscript under review for journal Wind Energ. Sci.
Published: 8 July 2016
© Author(s) 2016. CC-BY 3.0 License.

particularly in SNR, could be due to the different "hub heights" at each site; the SNR values shown for the BAO are from 100 m while the SNR values for the ARM site and wind farm are from 60 and 80 m, respectively. As SNR is strongly tied to aerosol concentrations, which generally decrease with height, SNR is expected to be lower for measurement heights that are further from the ground (e.g., Aitken et al., 2012). However, SNR values from the 50m height at the BAO were also generally lower than SNR values at the ARM site and wind farm. During the BAO campaign, much lower WC data availability was noted in comparison to the ARM site and wind farm campaigns. The lower data availability and SNR values at the BAO can be largely attributed to westerly flow from the direction of the Rocky Mountains, which brings cleaner air with a lower aerosol concentration to areas downwind of the mountains (Brown et al., 2013). Aitken et al. (2012) also noted lower WC lidar data availability in the Colorado foothills region in comparison to a site in Iowa.

TI is shown as a function of mean wind speed and stability class for the different sites in Fig. 6. Stability classes were stratified according to the value of α measured by the WC between 40 and 200 m, with thresholds given in Table 2. These thresholds are loosely based on the thresholds used in Wharton and Lundquist (2012). The shear parameter α was used as a proxy for stability in this work, as other stability parameters such as the Richardson number and Obukhov length require temperature measurements at different heights, which are not available from a lidar.

The Normal Turbulence Model (NTM; International Electrotechnical Commission, 2005), indicated by the black lines in Fig. 6, predicts a sharp decrease in TI as $\overline{U}$ increases and the denominator in Eq. 4 becomes larger. With the exception of some outliers, this trend is largely followed for the TI and $\overline{U}$ values at the different sites. At the ARM site and wind farm, TI values measured by the lidar are close to those predicted by the NTM under neutral conditions. At these sites, low shear conditions (near-zero or negative shear parameter) tended to be associated with low wind speeds and higher TI values. Low shear conditions often occur when the atmosphere is unstable, resulting in buoyant mixing, a uniform wind speed profile, and higher amounts of turbulence (e.g., Stull, 2000). In contrast, high shear conditions (large positive shear parameter) tended to be associated with higher wind speeds and lower TI values. High shear conditions often occur when the atmosphere is stable; mixing and turbulent motions are inhibited and wind speed tends to decrease with height as frictional effects from the surface become less dominant. At the BAO, low shear conditions were often associated with very low wind speeds and high TI, similar to the other sites. However, the striation of the $\overline{U}$/TI curve by shear parameter is not as prominent at the BAO, and high TI values were often associated with large shear parameters. At this site, the magnitude of TI is likely strongly affected by the low SNR values at the site (Fig. 5c) and complex terrain, in addition to the diurnal heating cycle. Thus, relations between TI, wind speed, and shear parameter are not as clear at the BAO.

Figures 5 and 6 demonstrate the large differences in atmospheric conditions and lidar data quality that can occur in different locations. Thus, the deployment of the same WC lidar at three different sites alongside met towers provides an excellent opportunity to assess the accuracy of lidar-measured TI at different locations. In addition, the large amount of lidar and met tower data collected during the experiments can be used to evaluate the effects of TI error on wind power prediction and to quantify the improvement in power prediction that occurs when lidar TI estimates are improved under different atmospheric conditions.

Wind Energ. Sci. Discuss., doi:10.5194/wes-2016-22, 2016
Manuscript under review for journal Wind Energ. Sci.
Published: 8 July 2016
© Author(s) 2016. CC-BY 3.0 License.

5 TI error and effects on power prediction

Scatter plots of met tower versus lidar 10min mean wind speed and TI for all three sites are shown in Fig. 7. Mean wind speeds measured by the lidar are extremely close to those measured by the met tower instruments, with regression line slopes near 1 and nearly all coefficient of determination (R^2) values greater than or equal to 0.99. There is slightly more scatter between the lidar and sonic mean wind speeds at the BAO (Fig. 7b), likely because SNR values at the BAO were lower and the lidar data quality was not as good in comparison to the other two sites. The excellent comparison of met tower and lidar mean wind speeds indicates that the WC lidar could accurately measure the mean flow at the different sites. However, large discrepancies between the TI measured by the lidar and the met tower instruments were noted at all three sites.

At the ARM site, α was strongly related to the sign of TI errors, with the WC overestimating TI under unstable conditions and underestimating TI under stable conditions (Fig. 7a). The over- and underestimation of TI was likely due to the effects of variance contamination and volume averaging, respectively. Regression line slopes increase with decreasing stability, as in Sathe et al. (2011). In this region of the United States, the shear parameter is strongly tied to the atmospheric stability (e.g., Newman and Klein, 2014), likely because the diurnal transition of the atmospheric layer largely controls the wind speed profile in flat terrain (e.g., Arya, 2001). TI error trends from the wind farm data set are remarkably similar to those found in the ARM data set (Fig. 7c). This is not surprising, as both data sets were collected in a similar region with similar terrain and diurnal transitions.

In contrast, lidar TI errors at the BAO did not follow a distinct pattern according to the shear parameter (Fig. 7b). Flow in this area is affected by complex terrain in addition to diurnal trends, so the shear parameter is likely not an accurate indicator of the atmospheric stability. At the BAO, nearly all the lidar TI measurements were overestimates in comparison to the sonic anemometers. As SNR values at the site were generally much lower in comparison to the ARM site (Fig. 5c), more noise was likely present in the lidar data at the BAO, resulting in TI overestimates. The lower SNR at the site also contributed to low lidar data availability and a much smaller number of data points in comparison to the other two sites.

Next, lidar and met tower TI data were used as inputs for the power prediction model, in addition to the hub-height wind speed, shear parameter, and turbine operating range. As discussed in Section 3.2, power was predicted for the 1.5MW WindPACT turbine, which has a hub height of 84 m and a rated wind speed of 11.5 m s^{-1}. Power error is expressed as a function of lidar TI error in Fig. 8, with different colored circles corresponding to different parts of the power curve. At all three sites, the largest power errors were found in the wind speed region just above and below the rated wind speed, where power sensitivity to turbulence is highest (Fig. 1b). In this region, even small TI errors of 1%–2% can result in power errors above 2.5% of the rated power. This trend is evident at all three sites, although there are relatively fewer points in this transition region at the BAO as a result of the lower mean wind speeds experienced at the BAO in comparison to the other two sites (Fig. 5a). The largest TI errors occur at lower wind speeds (near 75% of the rated wind speed). However, because power sensitivity to TI is low in this region of the power curve, these large TI errors did not often translate to large errors in predicted power. For wind speeds above the rated wind speed, power error increases steadily with increasing TI error, but most power errors are below 0.5% of the rated power.

Wind Energ. Sci. Discuss., doi:10.5194/wes-2016-22, 2016
Manuscript under review for journal Wind Energ. Sci.
Published: 8 July 2016
© Author(s) 2016. CC-BY 3.0 License.

Power percent error is expressed as a function of shear parameter and WC TI in Fig. 9. Atmospheric conditions range from low-shear, high TI environments at the upper left corner of the plots (i.e., unstable conditions) to high-shear, low-TI environments at the lower right corner of the plots (i.e., stable conditions). At all three sites, power errors are negligible for wind speeds near 75% of the rated wind speed and are generally smaller than 0.5% for wind speeds around 125% of the rated wind speed. The largest errors, as also shown in Fig. 8, occur for wind speeds near rated. (Note the small number of colored boxes in Fig. 9b for wind speeds near and above the rated wind speed. Colored boxes are only shown for bins with three or more data points, and wind speeds at the BAO were generally quite low, as previously discussed.) For the ARM site and the wind farm, the sign of the errors changes when moving from stable to unstable conditions, with power overestimates occurring under stable conditions and power underestimates occurring under unstable conditions. As the WC typically underestimates TI under stable conditions (Fig. 7), power predictions made with these TI estimates underestimate the effects of TI on power (Fig. 1a). Thus, power predictions made under stable conditions with the WC TI values are overestimates of the true power. In contrast, the WC overestimates TI under unstable conditions (Fig. 7) and thus overestimates the effect of TI on power. In the region near the rated wind speed, overestimating the TI results in predicting a lower amount of power than what is truly produced (Fig. 1a). At all three sites, the largest power errors tend to occur under low-shear, high TI conditions, which typically correspond to unstable conditions. This is not surprising, as WC TI estimates under unstable conditions had the largest errors in comparison to met tower measurements, as evidenced by the large slopes and lower R^2 values shown in Fig. 7.

6 Model results

In this section, initial results from L-TERRA are shown for data from the ARM site, the BAO, and the Southern Plains wind farm. For this initial investigation of the performance of L-TERRA, the structure function and six-beam techniques were not evaluated, as these techniques require further refinement for inclusion in the model.

6.1 Single data sets

First, data from each site were examined individually to assess model performance. For each site, all possible combinations of the error corrections described in Section 3.1 were evaluated. For the machine-learning module, 75% of the data were used for training with the remaining 25% used for testing model performance. The corrected lidar TI was then used as an input parameter for the power prediction model described in Section 3.2. Ten-minute mean power predicted from the lidar inputs was compared to power predicted from the met tower inputs, and the model combination that produced the lowest power mean absolute error (MAE) was selected as the optimal model combination for that particular site. At all three sites, data were filtered to avoid mast shadowing. In addition, 10min periods where the mean wind speed was less than 3 m s^{-1} were not used to evaluate L-TERRA, as the WindPACT turbine used in this work has a cut-in wind speed of 3 m s^{-1}.

The optimal model combinations for all three sites are shown in Table 3. (Note that only one variance contamination option was evaluated for this work, the correction based on Taylor's frozen turbulence hypothesis.) At all three sites, calculating the u, v, and w wind speed every 1 second using the DBS technique produced better results than calculating new values of the

Wind Energ. Sci. Discuss., doi:10.5194/wes-2016-22, 2016
Manuscript under review for journal Wind Energ. Sci.
Published: 8 July 2016
© Author(s) 2016. CC-BY 3.0 License.

wind speed components every 4 s using data from the entire scan. This is not surprising, as TI calculated from data with higher temporal resolution is more likely to match TI calculated from a cup or sonic anemometer. The noise removal, volume averaging, and machine-learning options were slightly different for the different sites. However, the use of corrected TI data in the power prediction model at all three sites significantly decreased power MAE values (Table 3).

Although L-TERRA improved lidar TI estimates and power predictions, the model does not perform uniformly under all atmospheric conditions. The change in power percent error resulting from application of L-TERRA is shown as a function of shear exponent and WC TI in Fig. 10 for the ARM site and Southern Plains wind farm (results from the BAO are not shown in this figure due to the smaller number of data points at the BAO). L-TERRA generally improves power estimates slightly for wind speeds above and below the rated wind speed, although the error increased for some periods with a small shear exponent (< 0.1). The largest decreases in power percent error occur for low TI values and higher shear exponent values at the ARM site (Fig. 10a), which typically correspond to stable conditions. The power percent error tended to increase for low shear (e.g., unstable conditions) at both sites, but particularly at the wind farm.

Scatter plots of WC versus met tower TI both before and after L-TERRA has been applied to the test set are shown in Fig. 11. Data points corresponding to an absolute power percent error greater than 1% are highlighted. Several periods with power percent error greater than 1% are associated with high-shear, low-TI conditions (stable). Although L-TERRA improves these TI estimates, bringing them very close to the one-to-one line (Figs. 11b, 11d), these periods are still associated with large power percent errors. This likely occurs because at both of these sites, low-TI, high-shear conditions often correspond to higher wind speeds near the rated wind speed of the 1.5MW WindPACT turbine (Figs. 6a, 6c), where turbulence sensitivity is highest (Fig. 1b). Other large power errors are associated with unstable and neutral conditions with higher TI values. Although the largest TI errors occur under low-shear, high-TI conditions (Figs. 7a, 7c, 11a, 11c), these large TI errors do not often result in large power errors, as they are usually associated with low wind speeds at both the ARM site and the wind farm (Figs. 6a, 6c), where turbulence sensitivity is low (Fig. 1b). Several of the neutral and unstable TI estimates that are associated with large power errors are initially located above the one-to-one line in Figs. 11a and 11c; these overestimates are likely a result of variance contamination, which is most prominent under unstable conditions (e.g., Sathe et al., 2011). The variance contamination module in L-TERRA reduces these TI overestimates somewhat, but several of the TI estimates associated with large power errors still lie above the one-to-one line in Figs. 11b and 11d. Some of the TI values measured by the WC under unstable conditions are initially quite accurate (e.g., the TI estimate lying on the one-to-one line near TI = 20% in Fig. 11a), but decrease as a result of the variance contamination module and become less accurate (Fig. 11b).

6.2 Combined data sets

In the previous section, the machine-learning model in L-TERRA was trained and tested at the same site and significantly reduced TI and power errors at all three sites. However, the goal of L-TERRA is to provide more accurate TI estimates from a stand-alone lidar at a site that does not have a met tower. Thus, the performance of L-TERRA at a site where the machine-learning model was not trained is of paramount importance.

Wind Energ. Sci. Discuss., doi:10.5194/wes-2016-22, 2016
Manuscript under review for journal Wind Energ. Sci.
Published: 8 July 2016
© Author(s) 2016. CC-BY 3.0 License.

In this section, the optimal physical corrections (Table 3) were applied to the data from each site. Data from each site were then divided into training and testing data sets, with 75% of the data used for training and 25% of the data used for testing, similar to the procedure used in Section 6.1. Different combinations of the training data sets were then used to train the MARS machine-learning model, and the trained model was tested on the test data sets from all three sites. The power MAE for each combination of training and testing sets is shown in Table 4, with bold values corresponding to model performance when the MARS model is both trained and tested at the same site.

For the ARM site, training the MARS model with the BAO and/or wind farm data always resulted in higher power MAE values in comparison to only training the model with data from the ARM site, although these MAE values were lower than the original MAE before L-TERRA was applied (Table 3). However, training the model with multiple data sets improved the performance of L-TERRA at the ARM site. When the BAO or wind farm training data sets were used individually, the power MAE for the ARM site was 2.13 kW. Training the model with data from both the BAO and the wind farm reduced the power MAE to 2.05 kW. By including data from different sites, the model can be trained on a larger variety of conditions and is thus more likely to perform better at a site where it has not been trained. Results for the BAO are similar, with lower power MAE values produced when both the ARM site and wind farm data are used to train the MARS model.

When the MARS model was trained using data from the ARM site and tested on the wind farm site, a large MAE value of 5.14 kW was produced (Table 4). This large increase in MAE is surprising, as the atmospheric conditions at the ARM site and the wind farm are quite similar (Figs. 5, 6). However, when the MARS model parameters were tuned to the ARM site data, the MAE value for the wind farm was reduced from 5.14 kW to 1.51 kW. Optimal tuning parameters for the different machine-learning models will be further investigated in the future when more data sets have been collected.

It should also be noted that while the MARS machine-learning model performed best for the ARM and BAO sites, a random forest model produced the lowest power MAE value for the wind farm (Table 3). Thus, different combinations of training and test sets were also evaluated with the random forest model. The use of a random forest instead of the MARS model reduced the wind farm MAE to 1.59 kW when the ARM training data set was used. However, using a random forest also increased the wind farm MAE to 11.95 kW when only the BAO training data set was used to train the model. Using a random forest increased the ARM site MAE to 5.84 kW when the BAO training data set was used. Thus, although the random forest model seems to generally perform better at the wind farm, large errors occur when only the BAO data set is used to train the random forest. It is possible that a random forest does not perform as well as the MARS model when the training data set is associated with different conditions than the testing data set (Fig. 5) or when the training data set is small. Histograms of training and testing input parameters indicated that several input parameters from the ARM and wind farm sites were outside the range of parameters used to train the model with the BAO data (not shown). This indicates the importance of using a training data set that encompasses a large range of atmospheric conditions.

In general, the machine-learning module in L-TERRA can be trained and tested at different sites without a significant increase in power MAE. This is an important finding, as it implies that L-TERRA can be trained at one or more sites and then applied to lidar data at a new site to improve TI estimates. While the MARS model performed well for the ARM and BAO data sets regardless of which training data sets were used, the random forest method was generally more well suited to the

Wind Energ. Sci. Discuss., doi:10.5194/wes-2016-22, 2016
Manuscript under review for journal Wind Energ. Sci.
Published: 8 July 2016
© Author(s) 2016. CC-BY 3.0 License.

wind farm data set. Future research will focus on the optimal machine-learning method to use for a particular combination of training and testing data sets.

7 Conclusions and future work

Lidars are currently being considered as a viable replacement to meteorological towers in the wind energy industry. Unlike met towers, lidars can be easily deployed at different locations and are capable of collecting wind speed measurements at heights spanning the entire turbine rotor disk. However, lidars measure different values of TI than a cup or sonic anemometer, and this uncertainty in lidar TI estimates is a major barrier to the adoption of lidars for wind resource assessment and power performance testing. In this work, a lidar turbulence error reduction model, L-TERRA, was developed and tested on WC lidar data from three different sites. The model incorporates both physics-based corrections and machine-learning techniques to improve lidar TI estimates.

Main findings from the work can be summarized as follows:

- For mean wind speeds near the rated wind speed of a turbine, small errors of 1%–2% in TI can result in large errors in power prediction.
- L-TERRA improves TI estimates and reduces power MAE at all three sites, although the optimal model configuration depends on the site.
- L-TERRA performs most poorly under high-shear conditions, when mean wind speeds tend to be near the rated wind speed, and under low-shear conditions, when variance contamination can significantly increase lidar TI estimates.
- The machine-learning module in L-TERRA generally reduces power MAE even when the machine-learning model is trained at one site and tested at another site. A larger reduction in MAE occurs when the machine-learning model is trained on more than one data set.

Although the combination of physics-based corrections and machine learning, as implemented in L-TERRA, is a promising method for reducing lidar TI error, further refinements must be made to different modules in the model to improve performance under a variety of conditions. Future work will include the use of a lidar simulator to improve the volume averaging and variance contamination corrections in L-TERRA. Additional data sets will be collected for training and testing of the model, including data sets from complex terrain and different areas of the world. The current version of L-TERRA was developed specifically for the vertically profiling WC lidar, but plans are underway to expand L-TERRA to different lidar models and scanning configurations.

The development of L-TERRA and other TI correction techniques has significant implications for the wind energy industry, which has traditionally relied on data from fixed met towers. L-TERRA can be applied to commercially available lidars that are commonly used in the wind industry, thus expanding the use of lidars for wind energy applications. Lidars with improved TI estimates can be used for wake studies, site classification, power curve testing, site monitoring, and resource assessment.

© Author(s) 2016. CC-BY 3.0 License.

Improved lidar TI estimates could also help wind energy developers make more informed decisions about turbine selection and wind farm layout. The use of lidars in place of met towers for wind energy applications should allow for more rapid development of wind in regions where it is difficult or costly to install met towers, and the improvement of lidar turbulence estimates will greatly assist in the adoption of lidars in the wind industry.

Acknowledgements. The authors would like to thank the staff of the Southern Great Plains ARM site, the BAO, and the Southern Plains wind farm, Tim Bonin, Bruce Bartram, and Daniel Wolfe of NOAA/ESRL, Lucas Root and Andreas Muschinski from NorthWest Research Associates, and Shiril Tichkule from the University of Colorado at Boulder for assisting with the lidar field deployments. Sebastien Biraud and Marc Fischer of Lawrence Berkeley National Laboratory supplied sonic anemometer data for the ARM site and Andreas Muschinski of NorthWest Research Associates provided sonic anemometer data for the BAO. Sonia Wharton of Lawrence Livermore National Laboratory provided the WINDCUBE lidar used in this work and assisted with field deployments. Leosphere and NRG Systems provided technical support for the WINDCUBE lidar during the experiments. Conversations with Caleb Phillips at NREL greatly enhanced our understanding of different machine learning models. The ARM Climate Research Facility is a U.S. Department of Energy Office of Science user facility sponsored by the Office of Biological and Environmental Research. This work was supported by the U.S. Department of Energy under Contract No. DE-AC36-08GO28308 with the National Renewable Energy Laboratory. Funding for the work was provided by the DOE Office of Energy Efficiency and Renewable Energy, Wind and Water Power Technologies Office.

The U.S. Government retains and the publisher, by accepting the article for publication, acknowledges that the U.S. Government retains a nonexclusive, paid-up, irrevocable, worldwide license to publish or reproduce the published form of this work, or allow others to do so, for U.S. Government purposes.

© Author(s) 2016. CC-BY 3.0 License.

References

Aitken, M. L., Rhodes, M. E., and Lundquist, J. K.: Performance of a wind-profiling lidar in the region of wind turbine rotor disks, J. Atmos. Oceanic Technol., 29, 347–355, doi:10.1175/JTECH-D-11-00033.1, 2012.

Arya, S. P.: Introduction to Micrometeorology, vol. 79 of *International Geophysics Series*, Academic Press, Cornwall, UK, 2nd edn., 2001.

Barthelmie, R. J., Crippa, P., Wang, H., Smith, C. M., Krishnamurthy, R., Choukulkar, A., Calhoun, R., Valyou, D., Marzocca, P., Matthiesen, D., Brown, G., and Pryor, S. C.: 3D wind and turbulence characteristics of the atmospheric boundary layer, Bull. Amer. Meteor. Soc., 95, 743–756, doi:10.1175/BAMS-D-12-00111.1, 2013.

Boquet, M., Callard, P., Deve, N., and Osler, E.: Return on investment of a lidar remote sensing device, DEWI Magazine, 37, 2010.

Branlard, E., Pedersen, A. T., Mann, J., Angelou, N., Fischer, A., Mikkelsen, T., Harris, M., Slinger, C., and Montes, B. F.: Retrieving wind statistics from average spectrum of continuous-wave lidar, Atmos. Meas. Tech., 6, 1673–1683, doi:10.5194/amt-6-1673-2013, 2013.

Brown, S. S., Thornton, J. A., Keene, W. C., Pszenny, A. A. P., Sive, B. C., Dubé, W. P., Wagner, N. L., Young, C. J., Riedel, T. P., Roberts, J. M., VandenBoer, T. C., Bahreini, R., Öztürk, F., Middlebrook, A. M., Kim, S., Hübler, G., and Wolfe, D. E.: Nitrogen, Aerosol Composition, and Halogens on a Tall Tower (NACHTT): Overview of a wintertime air chemistry field study in the Front Range urban corridor of Colorado, J. Geophys. Res.: Atmospheres, 118, 8067–8085, doi:10.1002/jgrd.50537, 2013.

Browning, K. A. and Wexler, R.: The determination of kinematic properties of a wind field using Doppler radar, J. Appl. Meteor., 7, 105–113, doi:10.1175/1520-0450(1968)007<0105:TDOKPO>2.0.CO;2, 1968.

Bulaevskaya, V., Wharton, S., Clifton, A., Qualley, G., and Miller, W. O.: Wind power curve modeling in complex terrain using statistical models, Journal of Renewable and Sustainable Energy, 7, 013 103, doi:10.1063/1.4904430, 2015.

Calhoun, R., Heap, R., Princevac, M., Newsom, R., Fernando, H., and Ligon, D.: Virtual towers using coherent Doppler lidar during the Joint Urban 2003 Dispersion Experiment, J. Appl. Meteor., 45, 1116–1126, doi:10.1175/JAM2391.1, 2006.

Chang, W. S.: Principles of Lasers and Optics, Cambridge University Press, 2005.

Clifton, A., Kilcher, L., Lundquist, J. K., and Fleming, P.: Using machine learning to predict wind turbine power output, Environmental Research Letters, 8, 024 009, doi:10.1088/1748-9326/8/2/024009, 2013.

Emeis, S.: Measurement Methods in Atmospheric Sciences: In-Situ and Remote, Borntraeger Science Publishers, 257 pp., 2010.

Friedman, J., Hastie, T., and Tibshirani, R.: The Elements of Statistical Learning, vol. 1, Springer Series in Statistics Springer, Berlin, 2001.

Friedman, J. H.: Multivariate adaptive regression splines, The Annals of Statistics, pp. 1–67, 1991.

Fuertes, F. C., Iungo, G. V., and Porté-Agel, F.: 3D turbulence measurements using three synchronous wind lidars: Validation against sonic anemometry, J. Atmos. Oceanic Technol., 31, 1549–1556, doi:10.1175/JTECH-D-13-00206.1, 2014.

Hogan, R. J., Grant, A. L., Illingworth, A. J., Pearson, G. N., and O'Connor, E. J.: Vertical velocity variance and skewness in clear and cloud-topped boundary layers as revealed by Doppler lidar, Quart. J. Roy. Meteor. Soc., 135, 635–643, doi:10.1002/qj.413, 2009.

Huffaker, R. M. and Hardesty, R. M.: Remote sensing of atmospheric wind velocities using solid-state and CO_2 coherent laser systems, Proceedings of the IEEE, 84, 181–204, 1996.

International Electrotechnical Commission: Wind turbines - Part 1: Design requirements, Tech. rep., IEC 61400-1, Geneva, Switzerland, 2005.

International Electrotechnical Commission: Wind turbines - Part 12-1: Power performance measurements of electricity producing wind turbines, Tech. Rep. Committee draft ed., IEC 61400-12-1, Geneva, Switzerland, 2013.

© Author(s) 2016. CC-BY 3.0 License.

Jonkman, B. J.: TurbSim user's guide: Version 1.50, Tech. Rep. No. TP-500-46198, National Renewable Energy Laboratory, Golden, Colorado, 2009.

Jonkman, J. M. and Buhl Jr., M. L.: FAST user's guide, Tech. Rep. No. NREL/EL-500-38230, National Renewable Energy Laboratory, Golden, CO, 2005.

Kaimal, J. and Finnigan, J.: Atmospheric Boundary Layer Flows: Their Structure and Measurement, Oxford University Press, 1994.

Kaimal, J. C. and Gaynor, J. E.: The Boulder Atmospheric Observatory, J. Climate Appl. Meteor., 22, 863–880, 1983.

Kolmogorov, A. N.: The local structure of turbulence in incompressible viscous fluid for very large Reynolds numbers, Doklady AN SSSR, 30, 301–304, 1941.

Krishnamurthy, R., Calhoun, R., Billings, B., and Doyle, J.: Wind turbulence estimates in a valley by coherent Doppler lidar, Meteorological Applications, 18, 361–371, doi:10.1002/met.263, 2011.

Krishnamurthy, R., Choukulkar, A., Calhoun, R., Fine, J., Oliver, A., and Barr, K.: Coherent Doppler lidar for wind farm characterization, Wind Energy, 16, 189–206, doi:10.1002/we.539, 2013.

Lenschow, D. H., Wulfmeyer, V., and Senff, C.: Measuring second-through fourth-order moments in noisy data, J. Atmos. Oceanic Technol., 17, 1330–1347, doi:10.1175/1520-0426(2000)017<1330:MSTFOM>2.0.CO;2, 2000.

Lundquist, J. K., Churchfield, M. J., Lee, S., and Clifton, A.: Quantifying error of lidar and sodar Doppler beam swinging measurements of wind turbine wakes using computational fluid dynamics, Atmos. Meas. Tech., 8, 907–920, doi:10.5194/amt-8-907-2015, 2015.

Malcolm, D. and Hansen, A.: WindPACT turbine rotor design study, Subcontract rep. No. SR-500-32495, National Renewable Energy Laboratory, Golden, CO, 2006.

Mann, J.: The spatial structure of neutral atmospheric surface-layer turbulence, J. Fluid Mech., 273, 141–168, doi:10.1017/S0022112094001886, 1994.

Mann, J., Peña, A., Bingöl, F., Wagner, R., and Courtney, M. S.: Lidar scanning of momentum flux in and above the atmospheric surface layer, J. Atmos. Oceanic Technol., 27, 959–976, doi:10.1175/2010JTECHA1389.1, 2010.

Mather, J. H. and Voyles, J. W.: The ARM Climate Research Facility: A review of structure and capabilities, Bull. Amer. Meteor. Soc., 94, 377–392, doi:10.1175/BAMS-D-11-00218.1, 2013.

Newman, J. F.: Optimizing lidar scanning strategies for wind energy turbulence measurements, Ph.D. thesis, University of Oklahoma, Norman, Oklahoma, USA, 2015.

Newman, J. F. and Klein, P. M.: The impacts of atmospheric stability on the accuracy of wind speed extrapolation methods, Resources, 3, 81–105, doi:10.3390/resources3010081, 2014.

Newman, J. F., Bonin, T. A., Klein, P. M., Wharton, S., and Newsom, R. K.: Testing and validation of multi-lidar scanning strategies for wind energy applications, Wind Energy, doi:10.1002/we.1978, 2016a.

Newman, J. F., Klein, P. M., Wharton, S., Sathe, A., Bonin, T. A., Chilson, P. B., and Muschinski, A.: Evaluation of three lidar scanning strategies for turbulence measurements, Atmos. Meas. Tech., 9, 1993–2013, doi:10.5194/amt-9-1993-2016, 2016b.

Newsom, R. K., Berg, L. K., Shaw, W. J., and Fischer, M. L.: Turbine-scale wind field measurements using dual-Doppler lidar, Wind Energy, 18, 219–235, doi:10.1002/we.1691, 2015.

Peña, A., Hasager, C. B., Gryning, S.-E., Courtney, M., Antoniou, I., and Mikkelsen, T.: Offshore wind profiling using light detection and ranging measurements, Wind Energy, 12, 105–124, doi:10.1002/we.283, 2009.

© Author(s) 2016. CC-BY 3.0 License.

Pichugina, Y. L., Tucker, S. C., Banta, R. M., Brewer, W. A., Kelley, N. D., Jonkman, B. J., and Newsom, R. K.: Horizontal-velocity and variance measurements in the stable boundary layer using Doppler lidar: Sensitivity to averaging procedures, J. Atmos. Oceanic Technol., 25, 1307–1327, doi:10.1175/2008JTECHA988.1, 2008.

Sathe, A. and Mann, J.: A review of turbulence measurements using ground-based wind lidars, Atmos. Meas. Tech., 6, 3147–3167, doi:10.5194/amt-6-3147-2013, 2013.

Sathe, A., Mann, J., Gottschall, J., and Courtney, M. S.: Can wind lidars measure turbulence?, J. Atmos. Oceanic Technol., 28, 853–868, doi:10.1175/JTECH-D-10-05004.1, 2011.

Sathe, A., Mann, J., Barlas, T., Bierbooms, W. A. A. M., and van Bussel, G. J. W.: Influence of atmospheric stability on wind turbine loads, Wind Energy, 16, 1013–1032, doi:10.1002/we.1528, 2013.

Sathe, A., Banta, R., Pauscher, L., Vogstad, K., Schlipf, D., and Wylie, S.: Estimating turbulence statistics and parameters from ground- and nacelle-based lidar measurements: IEA Wind expert report, DTU Wind Energy, Denmark, 2015a.

Sathe, A., Mann, J., Vasiljevic, N., and Lea, G.: A six-beam method to measure turbulence statistics using ground-based wind lidars, Atmos. Meas. Tech., 8, 729–740, doi:10.5194/amt-8-729-2015, 2015b.

Sjöholm, M., Mikkelsen, T., Mann, J., Enevoldsen, K., and Courtney, M.: Time series analysis of continuous-wave coherent Doppler lidar wind measurements, IOP Conference Series: Earth and Environmental Science, 1, 012 051, doi:10.1088/1755-1307/1/1/012051, 2008.

Sjöholm, M., Mikkelsen, T., Mann, J., Enevoldsen, K., and Courtney, M.: Spatial averaging-effects on turbulence measured by a continuous-wave coherent lidar, Meteor. Z., 18, 281–287, doi:10.1127/0941-2948/2009/0379, 2009.

Smola, A. J. and Schölkopf, B.: A tutorial on support vector regression, Statistics and Computing, 14, 199–222, doi:10.1023/B:STCO.0000035301.49549.88, 2004.

Sonnenschein, C. M. and Horrigan, F. A.: Signal-to-noise relationships for coaxial systems that heterodyne backscatter from the atmosphere, Appl. Opt., 10, 1600–1604, doi:10.1364/AO.10.001600, 1971.

Stawiarski, C., Träumner, K., Knigge, C., and Calhoun, R.: Scopes and challenges of dual-Doppler lidar wind measurements — An error analysis, J. Atmos. Oceanic Technol., 30, 2044–2062, doi:10.1175/JTECH-D-12-00244.1, 2013.

Strauch, R. G., Merritt, D. A., Moran, K. P., Earnshaw, K. B., and De Kamp, D. V.: The Colorado wind-profiling network, J. Atmos. Oceanic Technol., 1, 37–49, doi:10.1175/1520-0426(1984)001<0037:TCWPN>2.0.CO;2, 1984.

Stull, R. B.: Meteorology for Scientists and Engineers, Brooks/Cole, 2nd edn., 2000.

Vasiljevic, N., Courtney, M., and Mann, J.: A time-space synchronization of coherent Doppler scanning lidars for 3D measurements of wind fields, Ph.D. thesis, Denmark Technical University, Denmark, 2014.

Vickers, D. and Mahrt, L.: Quality control and flux sampling problems for tower and aircraft data, J. Atmos. Oceanic Technol., 14, 512–526, doi:10.1175/1520-0426(1997)014<0512:QCAFSP>2.0.CO;2, 1997.

Wagner, R., Antoniou, I., Pedersen, S. M., Courtney, M. S., and Jørgensen, H. E.: The influence of the wind speed profile on wind turbine performance measurements, Wind Energy, 12, 348–362, doi:10.1002/we.297, 2009.

Wainwright, C. E., Stepanian, P. M., Chilson, P. B., Palmer, R. D., Fedorovich, E., and Gibbs, J. A.: A time series sodar simulator based on large-eddy simulation, J. Atmos. Oceanic Technol., 31, 876–889, doi:10.1175/JTECH-D-13-00161.1, 2014.

Wharton, S. and Lundquist, J. K.: Assessing atmospheric stability and its impacts on rotor-disk wind characteristics at an onshore wind farm, Wind Energy, 15, 525–546, doi:10.1002/we.483, 2012.

Wharton, S., Newman, J. F., Qualley, G., and Miller, W. O.: Measuring turbine inflow with vertically-profiling lidar in complex terrain, J. Wind Eng. Ind. Aerodyn., 142, 217–231, doi:10.1016/j.jweia.2015.03.023, 2015.

Wind Energ. Sci. Discuss., doi:10.5194/wes-2016-22, 2016
Manuscript under review for journal Wind Energ. Sci.
Published: 8 July 2016
© Author(s) 2016. CC-BY 3.0 License.

Potential Predictor Variables	
Atmospheric State	**Lidar Operating Characteristics**
Corrected TI	SNR
σ_u^2	Instrument pitch
σ_w^2	Instrument roll
$\overline{U}$	Instrument internal temperature
α	
Horizontal wind speed dispersion	
Vertical wind speed dispersion	
Difference between lidar TI and IEC TI model	
Spectral broadening	
Wind direction	

Table 1. Potential predictor variables evaluated in the machine-learning module of L-TERRA.

Stability Classification	Shear Parameter Range
Strongly stable	$\alpha \geq 0.3$
Stable	$0.2 \leq \alpha < 0.3$
Neutral	$0.1 \leq \alpha < 0.2$
Unstable	$0 \leq \alpha < 0.1$
Strongly unstable	$\alpha < 0$

Table 2. Stability classifications used in this work.

Site	WS	Noise	Vol. Avg.	Var. Contam.	Machine Learning	MAE before (kW)	MAE after (kW)
ARM	1Hz DBS	Spike filter	Spectral fit	Taylor's hypothesis	MARS	2.16	1.77
BAO	1Hz DBS	Lenschow linear	ACF	Taylor's hypothesis	MARS	2.37	1.23
Wind Farm	1Hz DBS	Lenschow spectrum	ACF	Taylor's hypothesis	RF	1.64	1.32

Table 3. Optimal model options for different sites, with options shown for deriving wind speed (WS), noise corrections (Noise), volume averaging corrections (Vol. Avg.), variance contamination (Var. Contam.), and machine learning. Overall power MAE is shown both before and after L-TERRA has been applied.

Wind Energ. Sci. Discuss., doi:10.5194/wes-2016-22, 2016
Manuscript under review for journal Wind Energ. Sci.
Published: 8 July 2016
© Author(s) 2016. CC-BY 3.0 License.

	Testing Set		
Training Set	ARM	BAO	Wind Farm
ARM	**1.77**	1.45	5.14
BAO	2.13	**1.23**	1.96
Wind Farm	2.13	1.52	**1.56**
ARM + BAO	1.76	1.40	1.55
ARM + Wind Farm	1.83	1.36	1.43
BAO + Wind Farm	2.05	1.34	1.54

Table 4. Power MAE (in kW) for testing data sets from all three sites for different combinations of training data sets. The optimal physical corrections for each site (Table 3) and trained MARS model were applied to each testing data set to improve the TI estimates. The bold value in each column corresponds to the MAE value that results when the MARS model was trained and tested at the same site.

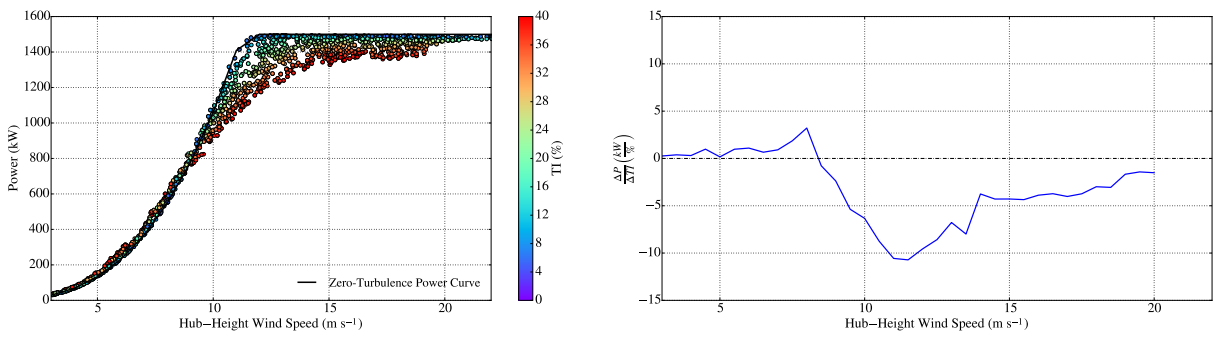

(a) (b)

Figure 1. a) Ten-minute mean power for the 1.5MW WindPACT turbine as a function of mean hub-height wind speed and TI. Mean power is derived from FAST simulations. Power curve where there is no turbulence in the flow ("zero-turbulence power curve") is shown for reference. Rated wind speed is 11.5 m s^{-1}. b) Sensitivity of power to TI as a function of mean hub-height wind speed for FAST simulations. Only data where the shear exponent is approximately equal to 0.2 are shown. Sensitivity was approximated as the regression line slope for power versus TI in different wind speed bins.

Wind Energ. Sci. Discuss., doi:10.5194/wes-2016-22, 2016
Manuscript under review for journal Wind Energ. Sci.
Published: 8 July 2016
© Author(s) 2016. CC-BY 3.0 License.

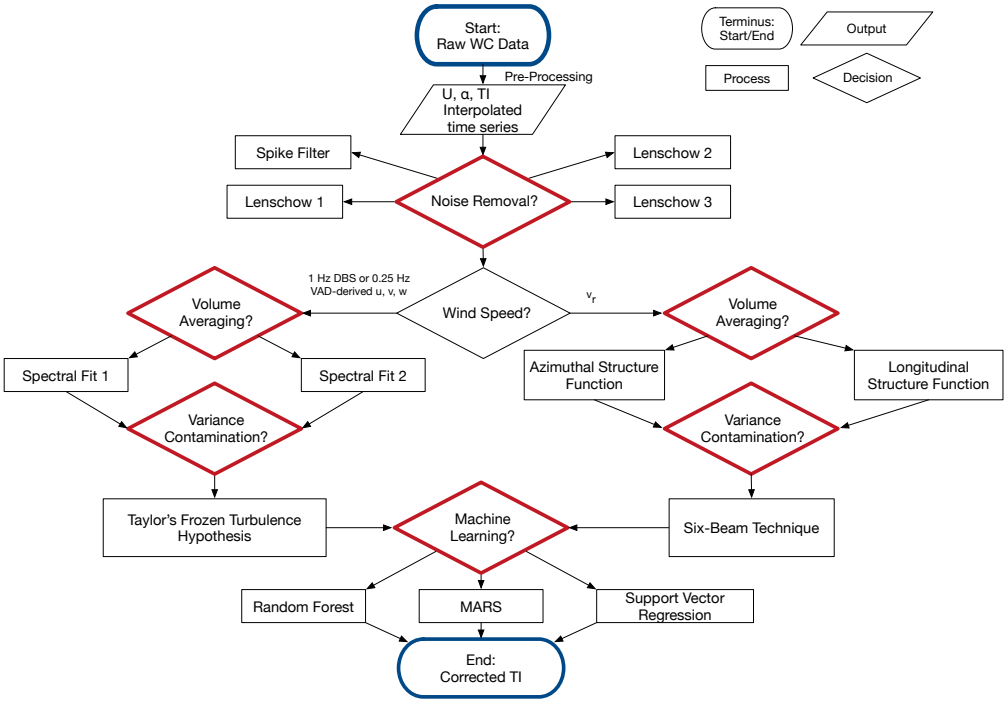

Figure 2. Flowchart depicting different methods for correcting TI with L-TERRA. Starting and ending points are indicated by blue-outlined ovals and modules are indicated by red-outlined diamonds.

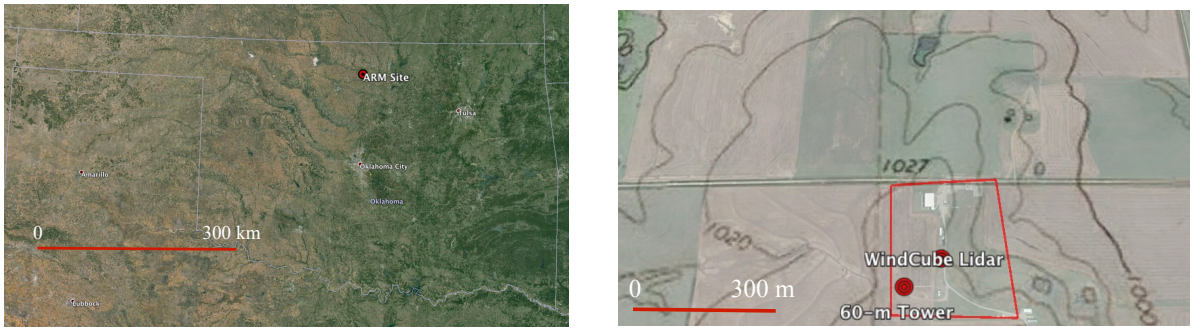

(a) (b)

Figure 3. (a) Google Earth image of the state of Oklahoma. Location of Southern Great Plains ARM site is denoted by red marker. (b) Google Earth image of the central facility of the Southern Great Plains ARM site (outlined in red box) with overlaid elevation contours in feet. Elevation map is from the United States Geological Survey and with contour intervals of approximately 10 feet (3.05 m). Locations of WC lidar and 60m tower are indicated by red circles.

Wind Energ. Sci. Discuss., doi:10.5194/wes-2016-22, 2016
Manuscript under review for journal Wind Energ. Sci.
Published: 8 July 2016
© Author(s) 2016. CC-BY 3.0 License.

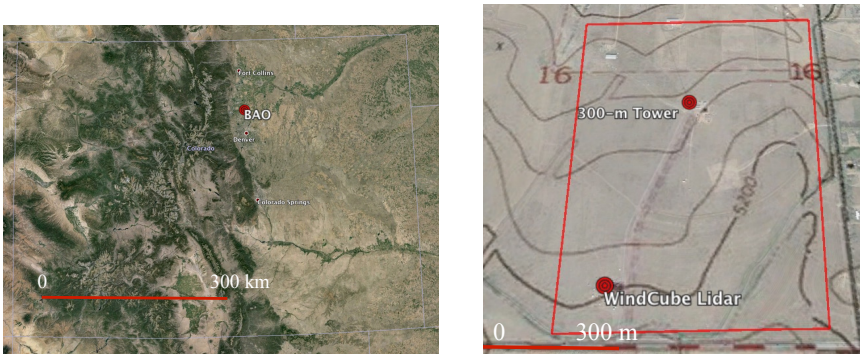

(a) (b)

Figure 4. a) Google Earth image of the state of Colorado. Location of BAO is denoted by red marker. (b) Google Earth image of the BAO (outlined in red box) with overlaid elevation contours in feet. Elevation map is from the United States Geological Survey and with contour intervals of approximately 10 feet (3.05 m). Locations of WC lidar and the 300m tower are indicated by red circles.

Wind Energ. Sci. Discuss., doi:10.5194/wes-2016-22, 2016
Manuscript under review for journal Wind Energ. Sci.
Published: 8 July 2016
© Author(s) 2016. CC-BY 3.0 License.

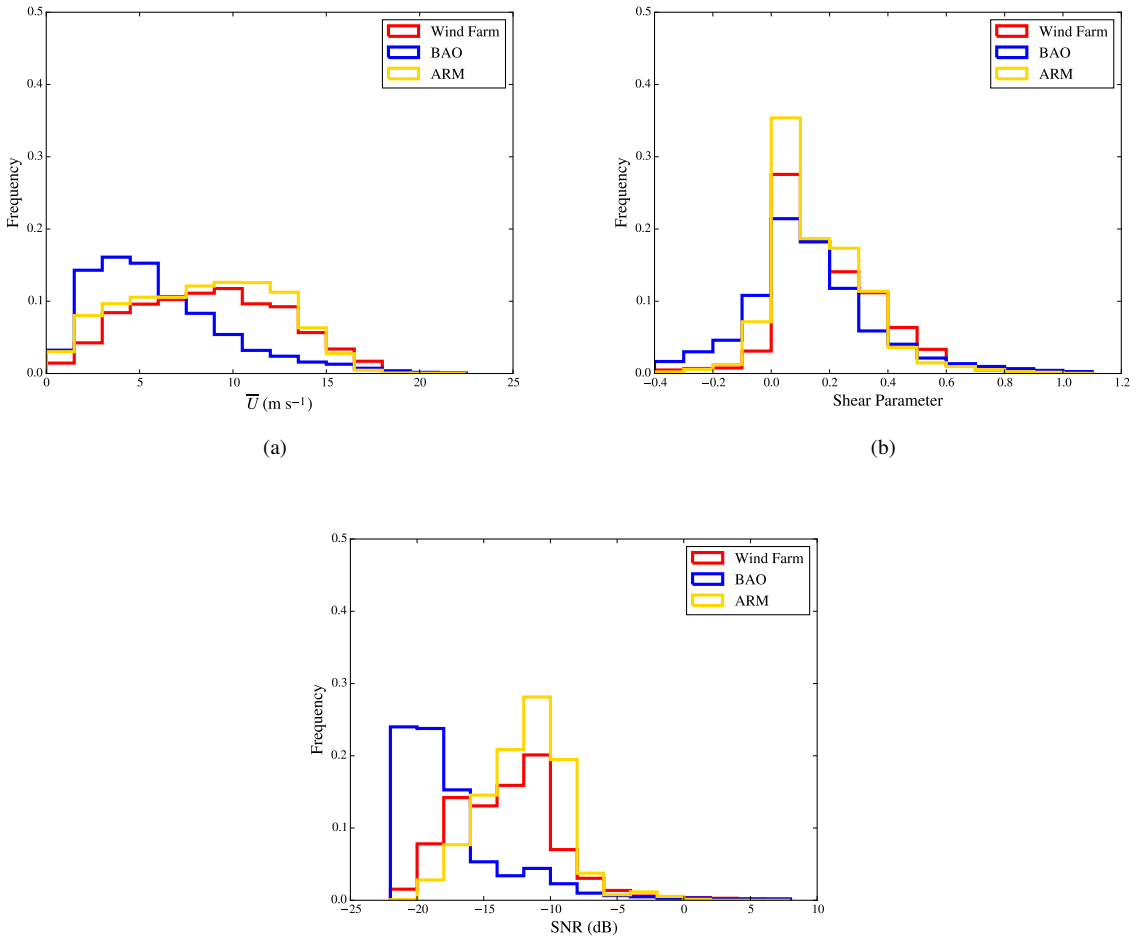

Figure 5. Histograms depicting relative frequency of values of a) $\overline{U}$ b) shear parameter and c) SNR at different sites.

Wind Energ. Sci. Discuss., doi:10.5194/wes-2016-22, 2016
Manuscript under review for journal Wind Energ. Sci.
Published: 8 July 2016
© Author(s) 2016. CC-BY 3.0 License.

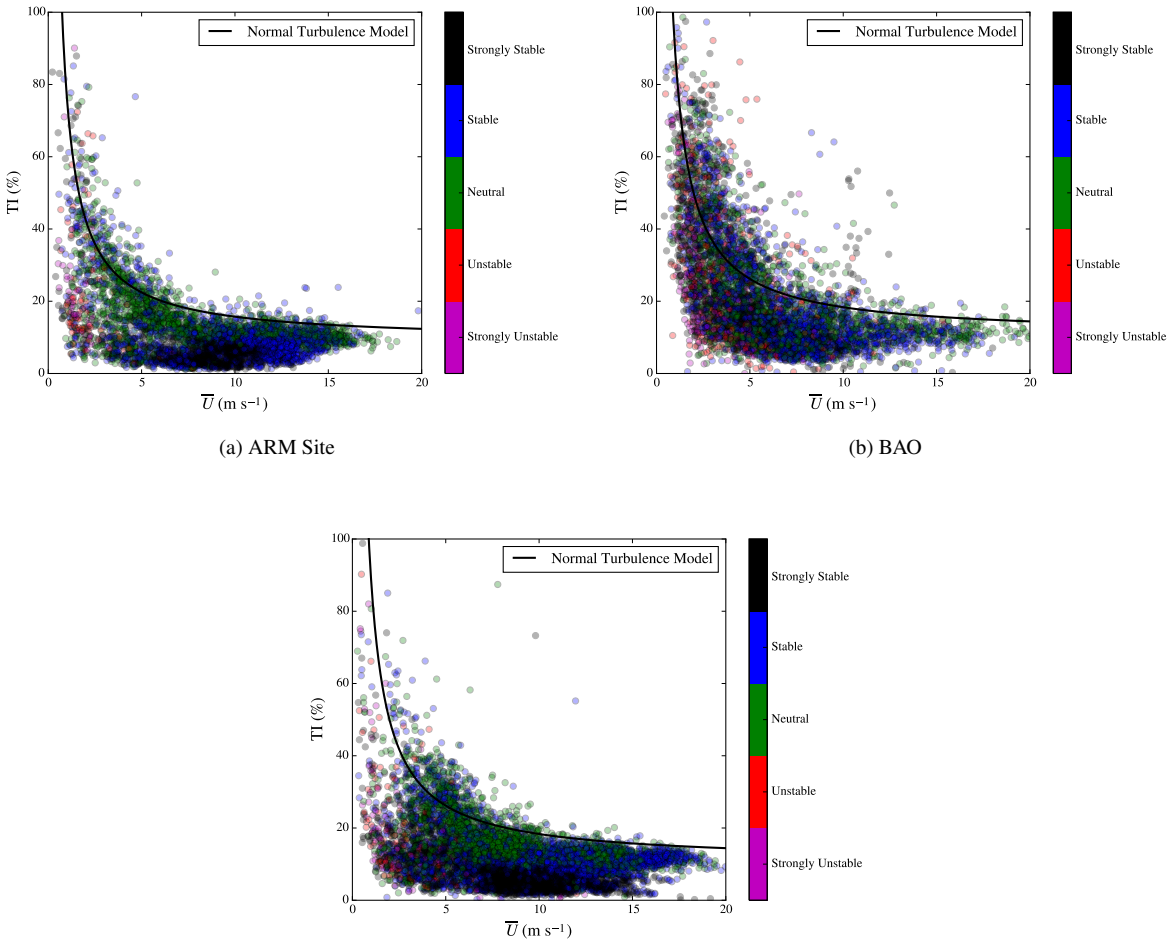

(a) ARM Site

(b) BAO

(c) Wind Farm

Figure 6. WC TI as a function of mean wind speed at the a) ARM site, b) BAO, and c) Southern Plains wind farm. Colored circles indicate different stability classifications, as defined in Table 2. Values of TI derived from the Normal Turbulence Model (International Electrotechnical Commission, 2005) are also shown.

Wind Energ. Sci. Discuss., doi:10.5194/wes-2016-22, 2016
Manuscript under review for journal Wind Energ. Sci.
Published: 8 July 2016
© Author(s) 2016. CC-BY 3.0 License.

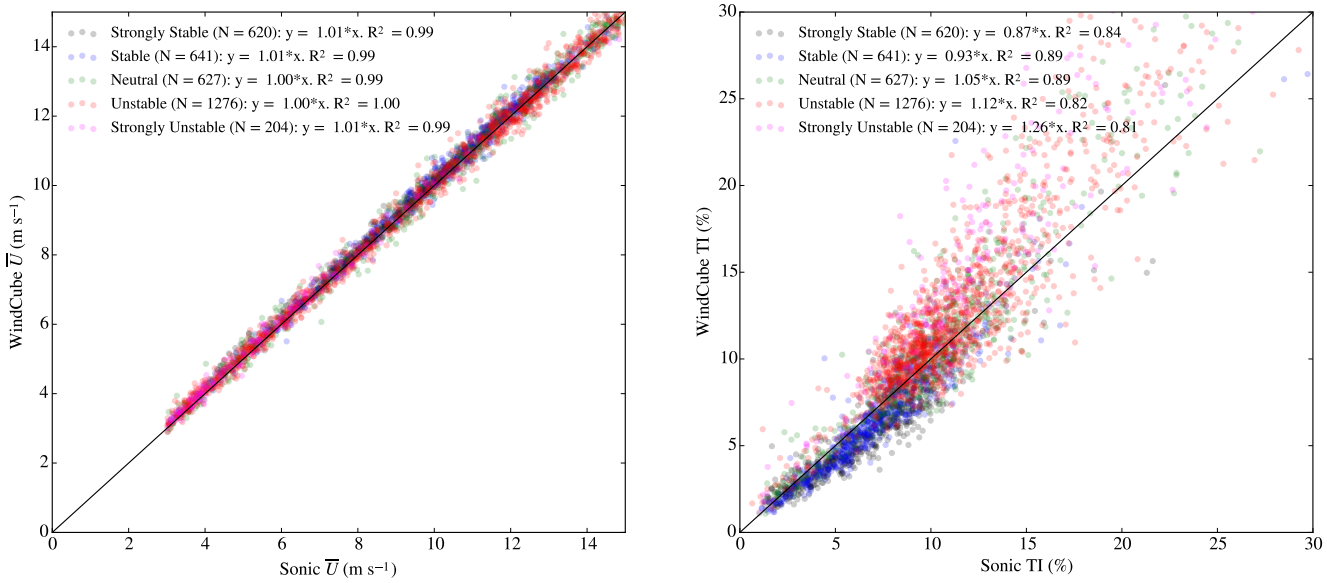

(a) ARM Site

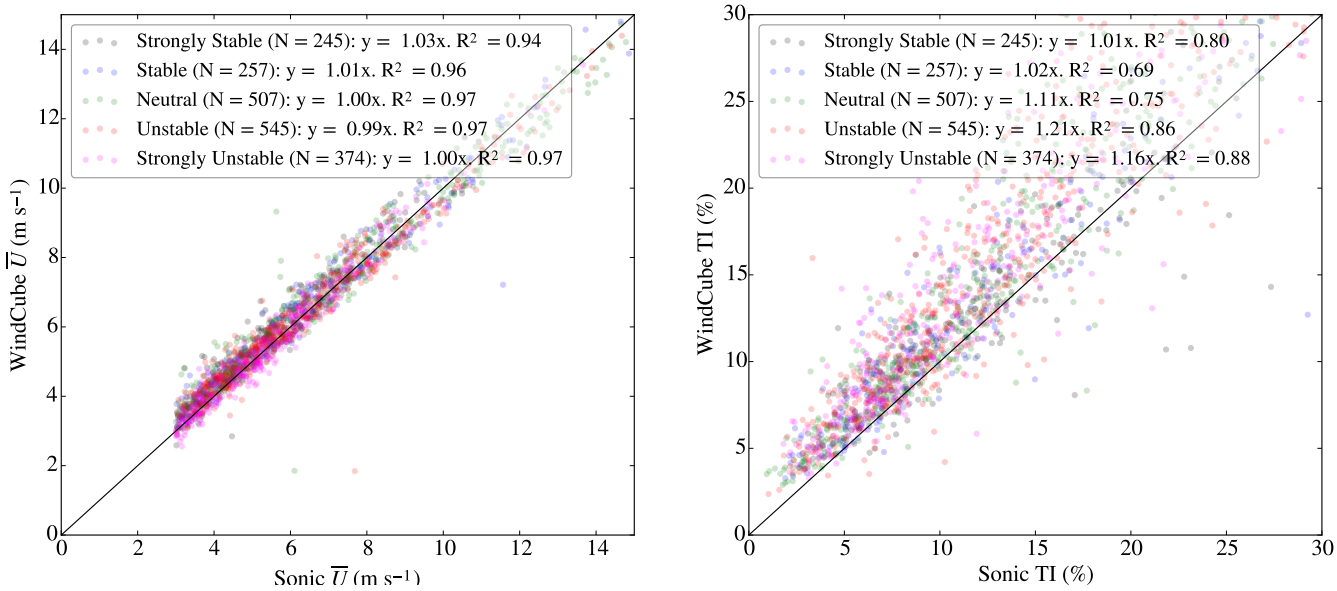

(b) BAO

Figure 7. Met tower vs. WC lidar mean wind speed (left panels) and TI (right panels) for data from a) ARM site, b) BAO, and c) Southern Plains wind farm. Stability is classified by shear parameter as described in the text. One-to-one lines are shown for reference, and regression line equations for each stability category are shown in figure legends. Note that only data where $\overline{U} > 3$ m s^{-1} were used in this work. (Figure continues on next page.)

Wind Energ. Sci. Discuss., doi:10.5194/wes-2016-22, 2016
Manuscript under review for journal Wind Energ. Sci.
Published: 8 July 2016
© Author(s) 2016. CC-BY 3.0 License.

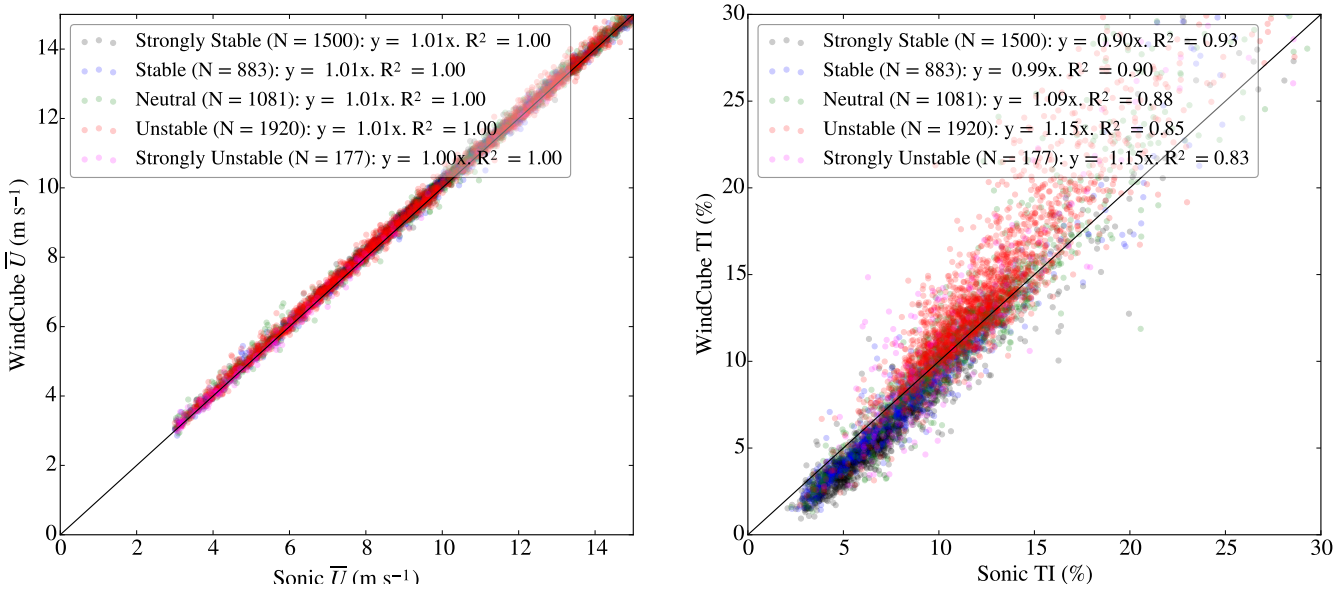

(c) Wind Farm

Figure 7. (continued)

Wind Energ. Sci. Discuss., doi:10.5194/wes-2016-22, 2016
Manuscript under review for journal Wind Energ. Sci.
Published: 8 July 2016
© Author(s) 2016. CC-BY 3.0 License.

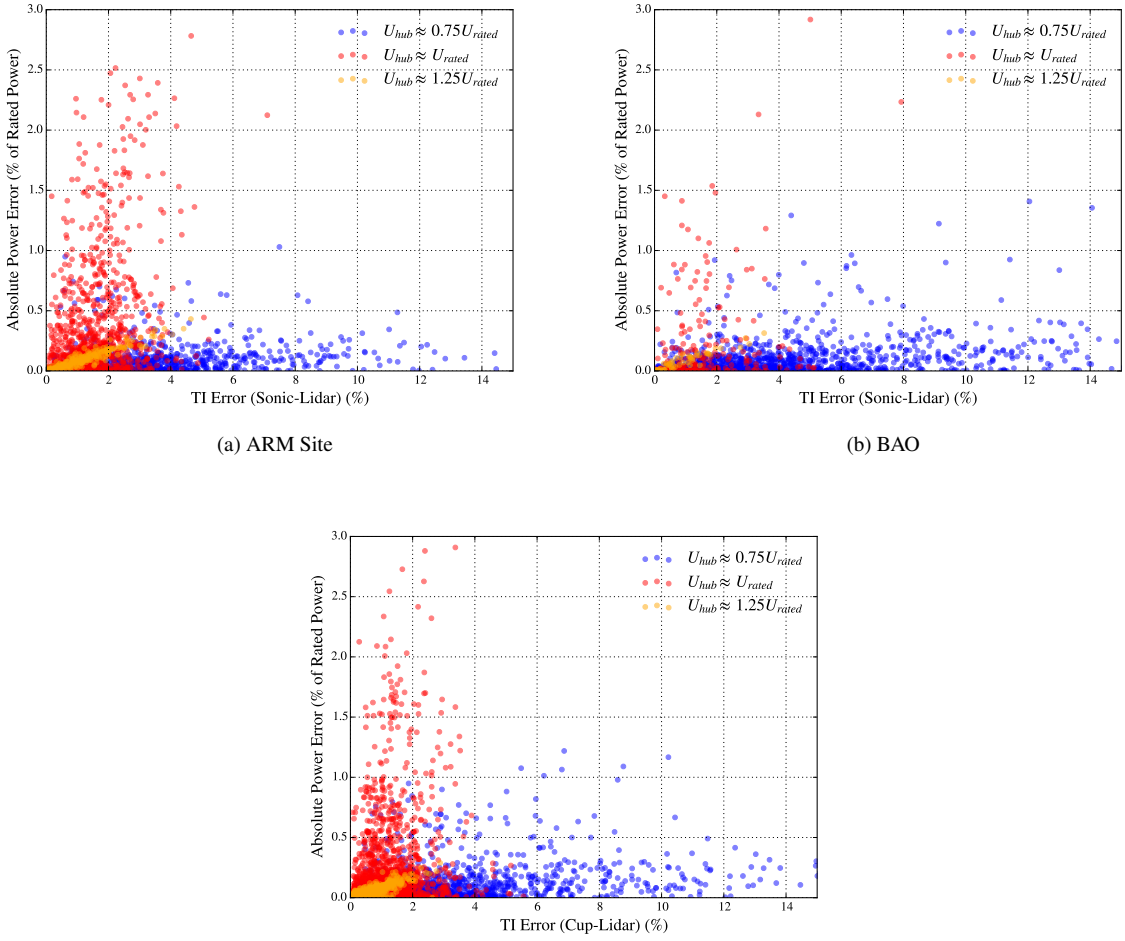

(a) ARM Site

(b) BAO

(c) Wind Farm

Figure 8. Absolute power error from random forest model (expressed as a percentage of rated power) as a function of lidar TI error. Results are shown for a) ARM site, b) BAO, and c) Southern Plains wind farm.

Wind Energ. Sci. Discuss., doi:10.5194/wes-2016-22, 2016
Manuscript under review for journal Wind Energ. Sci.
Published: 8 July 2016
© Author(s) 2016. CC-BY 3.0 License.

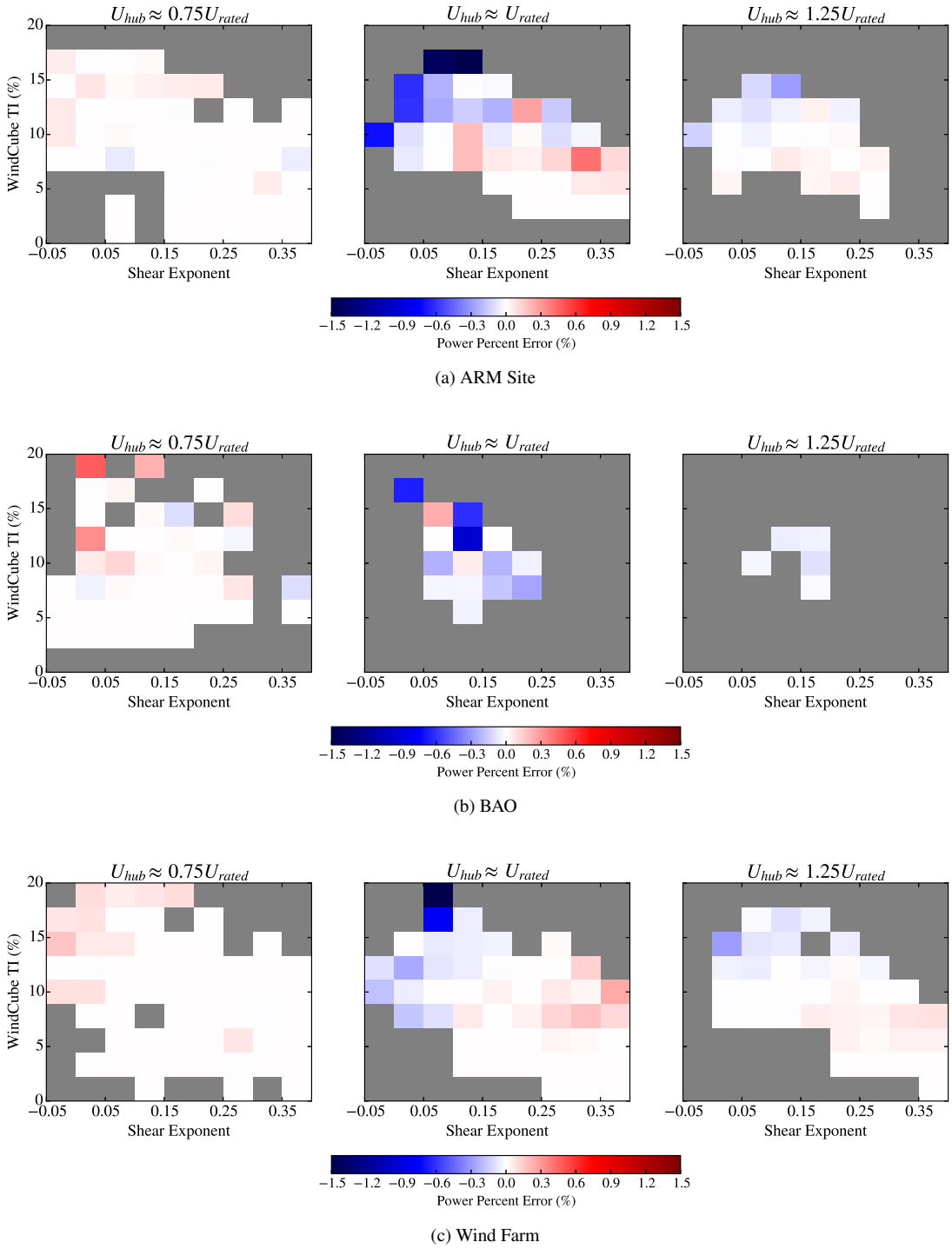

Figure 9. Median power percent error for different shear parameter and TI bins for three wind speed regions. Results are shown for a) ARM site, b) BAO, and c) Southern Plains wind farm. Red squares represent power overestimates while blue squares represent power underestimates.

Wind Energ. Sci. Discuss., doi:10.5194/wes-2016-22, 2016
Manuscript under review for journal Wind Energ. Sci.
Published: 8 July 2016
© Author(s) 2016. CC-BY 3.0 License.

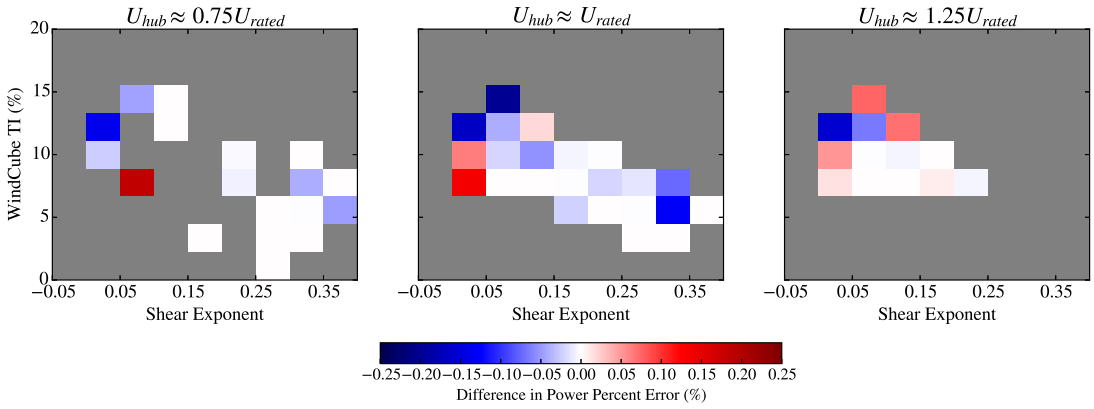

(a) ARM Site

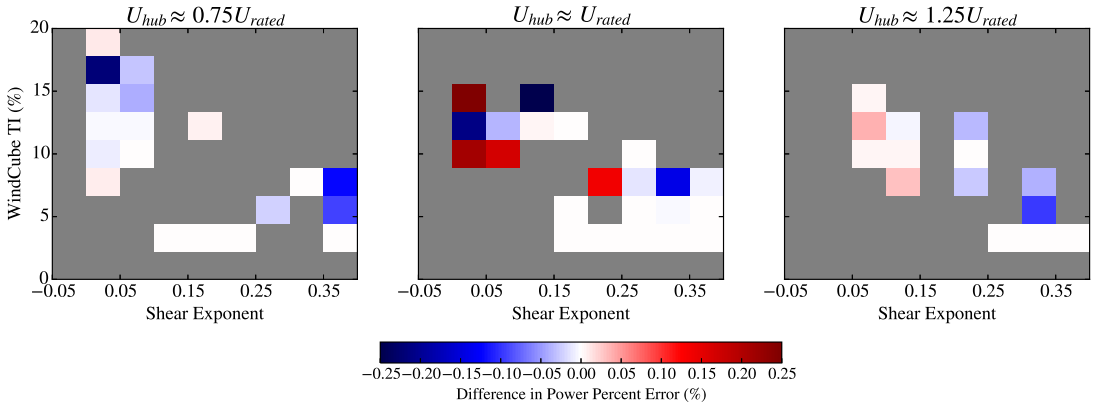

(b) Wind Farm

Figure 10. Median change in power percent error for different shear parameter and TI bins for three wind speed regions after L-TERRA has been applied. Results are shown for a) ARM site and b) Southern Plains wind farm. Red squares represent increases in power percent error while blue squares represent decreases in power percent error. Note that results are not shown for the BAO due to the small number of data points in the test sample from the BAO.

Wind Energ. Sci. Discuss., doi:10.5194/wes-2016-22, 2016
Manuscript under review for journal Wind Energ. Sci.
Published: 8 July 2016
© Author(s) 2016. CC-BY 3.0 License.

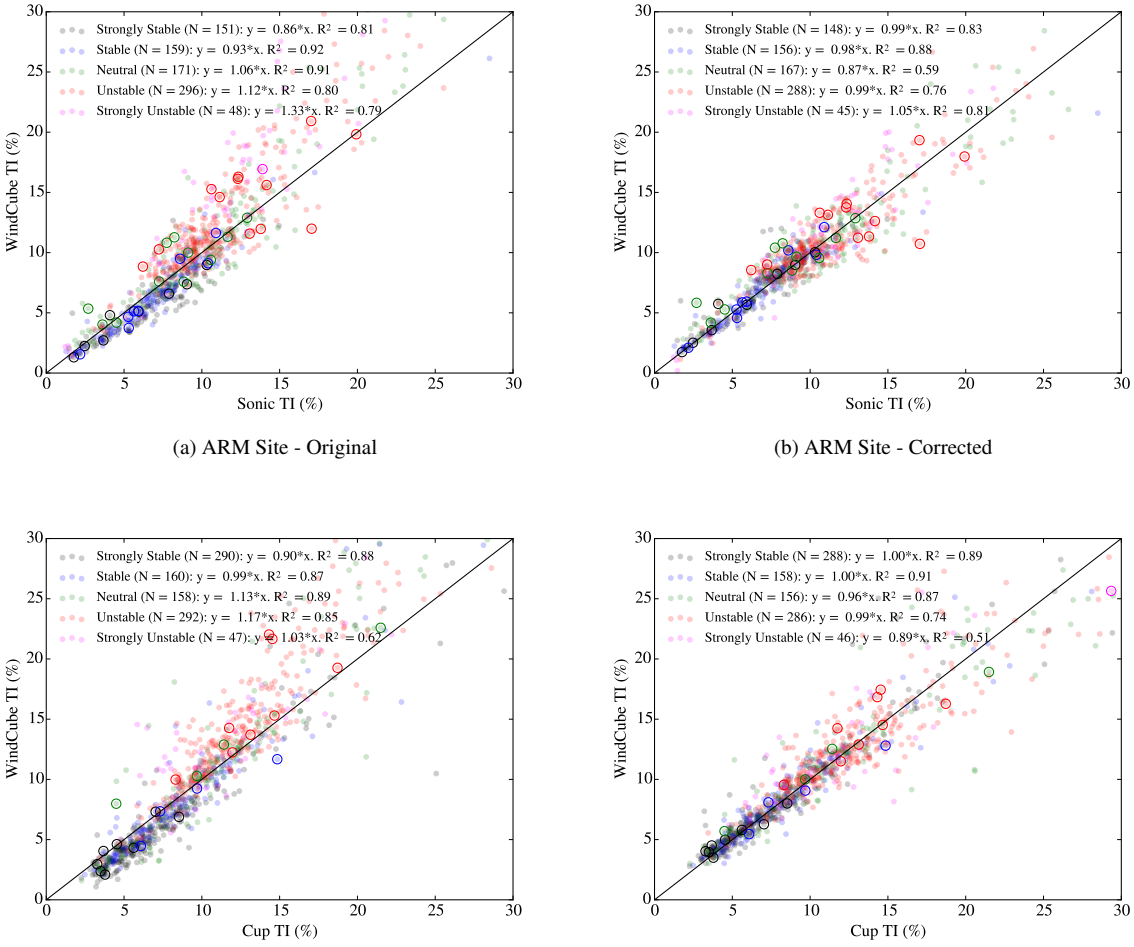

(a) ARM Site - Original

(b) ARM Site - Corrected

(c) Wind Farm - Original

(d) Wind Farm - Corrected

Figure 11. Met tower vs. WC lidar TI for data from a) and b) ARM site and c) and d) Southern Plains wind farm. Left panels show original WC TI and right panels show corrected WC TI. Outlined points correspond to times when the absolute power percent error was greater than 1% after L-TERRA was applied.